NANO REVIEW   **Open Access**

Progress in Iron Oxides Based Nanostructures for Applications in Energy Storage

Linfeng Lv[1,2], Mengdi Peng[1,2], Leixin Wu[1], Yixiao Dong[2], Gongchuan You[1], Yixue Duan[1,2], Wei Yang[2], Liang He[1,2,3] and Xiaoyu Liu[1*]

Abstract

The demand for green and efficient energy storage devices in daily life is constantly rising, which is caused by the global environment and energy problems. Lithium-ion batteries (LIBs), an important kind of energy storage devices, are attracting much attention. Graphite is used as LIBs anode, however, its theoretical capacity is low, so it is necessary to develop LIBs anode with higher capacity. Application strategies and research progresses of novel iron oxides and their composites as LIBs anode in recent years are summarized in this review. Herein we enumerate several typical synthesis methods to obtain a variety of iron oxides based nanostructures, such as gas phase deposition, co-precipitation, electrochemical method, etc. For characterization of the iron oxides based nanostructures, especially the in-situ X-ray diffraction and ^{57}Fe Mössbauer spectroscopy are elaborated. Furthermore, the electrochemical applications of iron oxides based nanostructures and their composites are discussed and summarized.

Keywords: Iron oxide, Nanostructure, Lithium-ion battery, Anode

Introduction

The global energy and environment problems lead to increasing demand for highly efficient green energy, e.g., solar energy, fuel cells, lithium-ion batteries (LIBs) and thermoelectric module, etc. [1–11]. Research and development of high-performance and low-cost energy storage system is an important solution for these problems. Among the energy storage devices with wide applications, LIBs are an important candidates for highly effective energy storage system [12–24]. However, the current commercial graphite anode has the limitations, e.g., a relatively low theoretical capacity (372 mA h g^{-1}), and some electrochemically active materials are proposed to be applied in LIBs [25–29]. In 2000, Poizot et al. [30] reported that the transition metal oxides (TMOs)

are considered as a kind of important anodes in LIBs since their high theoretical capacities 2–3 times that of graphite. Therefore, TMOs and related composites are attracting much attention as LIBs anode. During lithium insertion/extraction process, TMOs have the following reaction [31].

$$M_xO_y + 2ye^- + 2y\text{Li}^+ \leftrightarrow x\text{M}^0 + y\text{Li}_2\text{O} \tag{1}$$
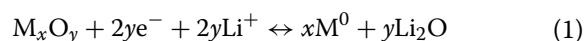
where, M represent Ni, Cu, Fe, Co, etc. During the lithium insertion process, these oxides are reduced by lithium, and the composite consisting of metallic clusters dispersed in a matrix of amorphous Li_2O is formed [30, 31].

Among TMOs, iron oxides based anodes are one kind of excellent candidates with great potential in LIBs since they possess such advantages, e.g., abundance, low cost and nontoxicity [32, 33]. However, as similar as other TMOs, iron oxides serving as LIBs anode have two critical issues. One is the large irreversible capacity, caused

*Correspondence: liuxiaoyu@scu.edu.cn
[1] School of Mechanical Engineering, Sichuan University, Chengdu 610065, People's Republic of China
Full list of author information is available at the end of the article

Lv *et al. Nanoscale Res Lett* (2021) 16:138

Page 2 of 19

by decomposition of electrolyte and formation of solid electrolyte interface (SEI) layer in the 1st discharge process. Additionally, the formation of Fe and Li_2O is thermodynamically feasible, and the extraction of lithium ion (Li^+) from Li_2O is thermodynamically instable [34], since a part of Li^+ cannot be extracted from Li_2O formed in the 1st discharge process. This also results in partial irreversible capacity. Another issue is their low cycling stability mainly resulted from a large volume variation and severe aggregation of Fe in insertion/deinsertion of Li^+, leading to pulverization of electrodes and rapid decay in capacity [3]. For solution to these problems, much effort is focusing on overcoming these issues and some highly effective approaches are proposed. To the best of our knowledge, one highly-effective strategy is nanostructuring of iron oxides [3, 35]. For some unique nanostructures, the strain and volume variation resulted from insertion/deinsertion of Li^+ will be inhibited at large extent, also the Li^+ can be diffused in electrodes easily, leading to significantly improved electrochemical performance of the anode [11]. Furthermore, carbonaceous materials, e.g., carbon fibers (CFs), carbon nanotubes (CNTs), graphene, and pyrolyzed carbon, etc. are introduced for compositing with iron oxides [36–38]. The volume variation of composite electrodes in charge/discharge can be buffered by these carbonaceous materials with unique structures, hence the electronic contact and the cycling stability of iron oxides nanostructures are increased.

In this review, the recently developed strategies and important research updates on the iron oxides ($Fe_{1−x}O$, Fe_2O_3, Fe_3O_4) based nanostructures with applications in LIBs and supercapacitors are elaborated and summarized. Specifically, we concentrated on the iron oxides based nanostructure's synthesis and design, as well as their electrochemical performance.

Wustite (Fe$_{1−x}$O)

Wustite ($Fe_{1−x}O$) is a non-stoichiometric compound with $0 < x < 0.0464$ [11]. It has the rocksalt cubic structure, and its lattice constant is ~ 4.330 Å [11]. $Fe_{1−x}O$, compared with Fe_2O_3 and Fe_3O_4, has less applications in energy storage since its relatively low specific capacity and metastable phase below 843.15 K which tends to decompose into Fe and Fe_3O_4. However, $Fe_{1−x}O$, a highly promising anode for LIBs, has a higher electrical conductivity than those of Fe_2O_3 and Fe_3O_4.

Synthesis and Characterization

As far as we know, the compositing of TMOs with high-performance coverage has great potential for high-performance LIBs anode [7]. In LIBs, the electrochemical mechanism of wustite anode is described as the following equation [8].

$$FeO + 2Li^+ + 2e^- \leftrightarrow Fe + Li_2O \qquad (2)$$
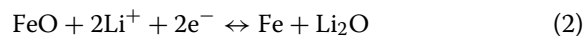
FeO/C composites were synthesized using a facile method by Gao et al. [31]. In their synthesis, $α-Fe_2O_3$ particles with size of 30–120 nm were mixed with acetylene black (AB) of different percentages, and a uniform mixture was obtained by ball milling. Then, the mixture of $α-Fe_2O_3$ and AB was carbonthermally reduced at 800 °C for 10 h in N_2 atmosphere to obtain uniform FeO/C composites. The FeO/C composite possesses much higher cycling stability than that of Fe_2O_3/AB mixture. When the content of AB is 50 wt.%, the capacity of FeO/C composite is 511 mA h $g^{−1}$, higher than 396 mA h $g^{−1}$ of Fe_2O_3/AB. Besides, the capacity retention after 50 cycles is > 96%, obviously 70–80% higher than that of Fe_2O_3/AB. It is believable that the superior electrochemical performance of FeO/C composite should be resulted from its higher electrical conductivity, resulted from strengthened connection of the FeO and AB particles after carbonthermal reduction.

Afterward, in 2016, Jung et al. [11] prepared a potassium (K)-FeO/graphene composite as LIBs anode based on K-doped FeO nanoparticles by thermal diffusion of K into Fe_2O_3/graphene using polyol reduction. Rhombohedral Fe_2O_3 crystals were transformed into FeO crystals (face-centered cubic, FCC), showing a broad d-spacing (5.2 Å) of (111) crystal planes, by calcination of K-doped Fe_2O_3/graphene. Comparing with previously studied Fe_2O_3/graphene composite [11], the K-FeO/graphene showed a discharge capacity of 1776 mA h $g^{−1}$ with high cycling stability during 50 cycles at a current density of 100 mA $g^{−1}$, whereas Fe_2O_3/graphene delivered a discharge capacity of 1569 mA h $g^{−1}$. Even at a high current density of 18.56 A $g^{−1}$, the capacity of K-FeO/graphene remained at 851 mA h $g^{−1}$ after 800 cycles. This difference is much larger after the electrodes are cycled longer at a high current density of 18.56 A $g^{−1}$. As shown in Fig. 1, compared with the Fe_2O_3/graphene, the K-FeO/graphene anode has unique crystal structure and reaction mechanism. The high discharge capacity of K-FeO/graphene indicates that specific capacity by storage of additional Li^+ should be contributed from the vacancies and broad d-spacing within Wustite lattices through potassium diffusion into Fe_2O_3 lattices.

In-Situ X-ray Diffraction

By in-situ X-ray diffraction (XRD), the information of real-time structural change during the reaction process of sample, and a large amount of comparable information can be obtained in a short period. It can not only observe the structural change of sample during the synthesis process, it also can be used to detect the corresponding structural change of sample at different temperatures
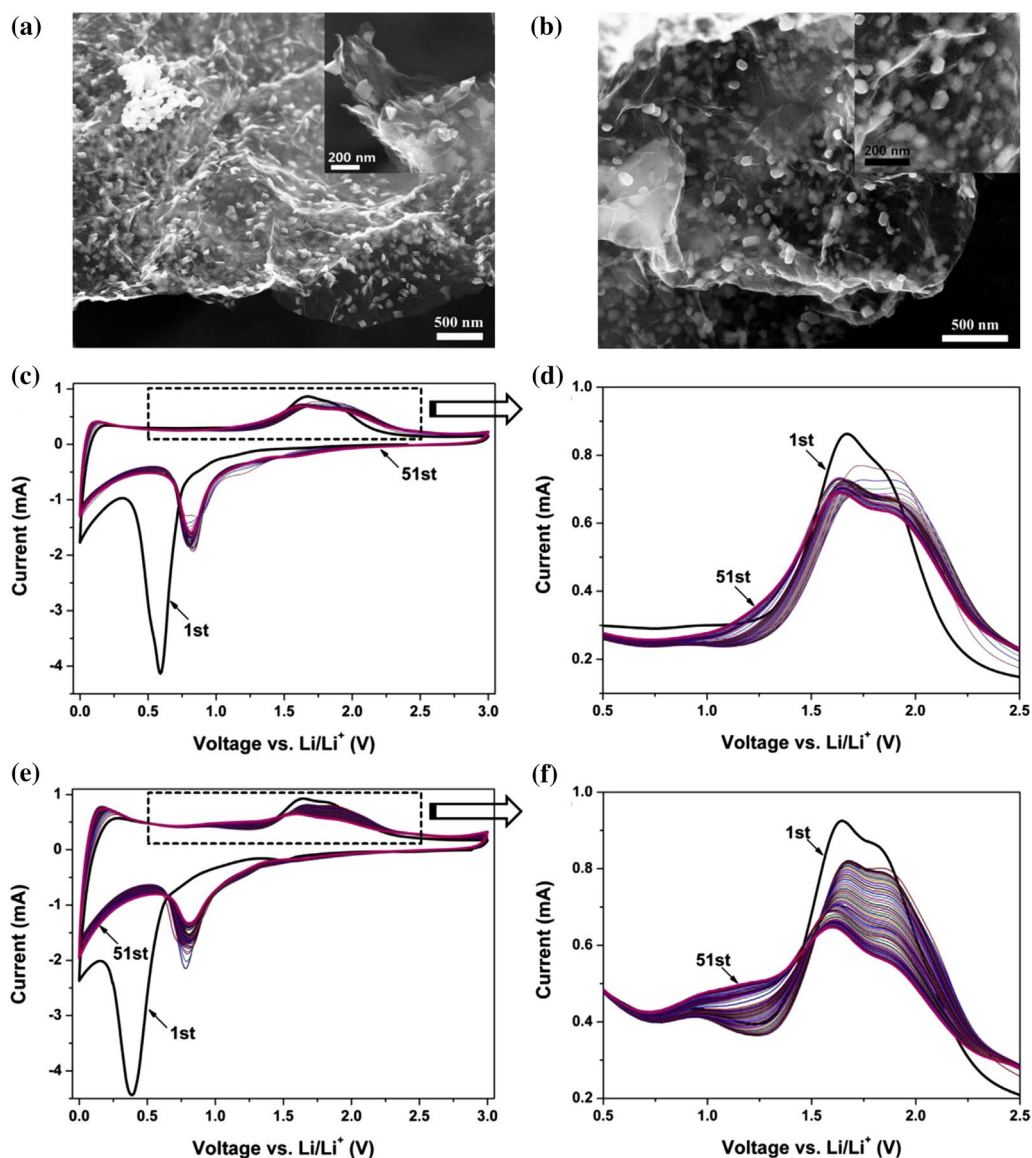
Lv *et al. Nanoscale Res Lett* (2021) 16:138

Page 3 of 19

Fig. 1 SEM images of **a** Fe$_2$O$_3$/graphene and **b** K-FeO/graphene, and the inset in (**a**, **b**) are their magnified images, respectively. Repeated cyclic voltammograms of **c**, **d** the Fe$_2$O$_3$/graphene electrode and **e**, **f** the K-FeO/graphene electrode. Two electrodes were continually scanned for the 51st cycles with a potential sweep rate of 0.5 mV s^{-1}. Reprinted with Permission from [11]. Copyright, Elsevier B.V

under charge/discharge to a certain potential, which is highly useful for monitoring the actual reaction mechanism of anode/cathode in battery. In addition, our group studied precise knowledge of wustite's lattice constant that is required for the investigation of its physical and chemical properties at high temperature. The Fe$_{1-x}$O was synthesized and characterized by high temperature X-ray diffractometer (RINT2000-TTR, Rigaku Denki Co., Ltd.) with parallel beams (Fig. 2a) for measuring the specific diffraction peaks, and the relation between the composition and lattice constant of wustite at high temperature

is also investigated. The synthesis process of wustite with the α-Fe (95 wt.%) and Fe$_3$O$_4$ (99 wt%) powders as initial materials is a eutectoid reaction (Fig. 2b). This reaction can be proceeded between 843.15 and 1673.15 K at certain Pco/Pco$_2$ since the wustite is unstable below 843.15 K, and the reactants are 19% Fe (wt.%) and 81% Fe$_3$O$_4$ (wt.%). Figure 2c shows the XRD pattern of initial reactants (magnetite and iron). Experiment condition is described in Table 1. After purging Helium (He) gas (25 ml min^{-1}) into the furnace of XRD system for 60 min, the reactants were heated with a constant rate
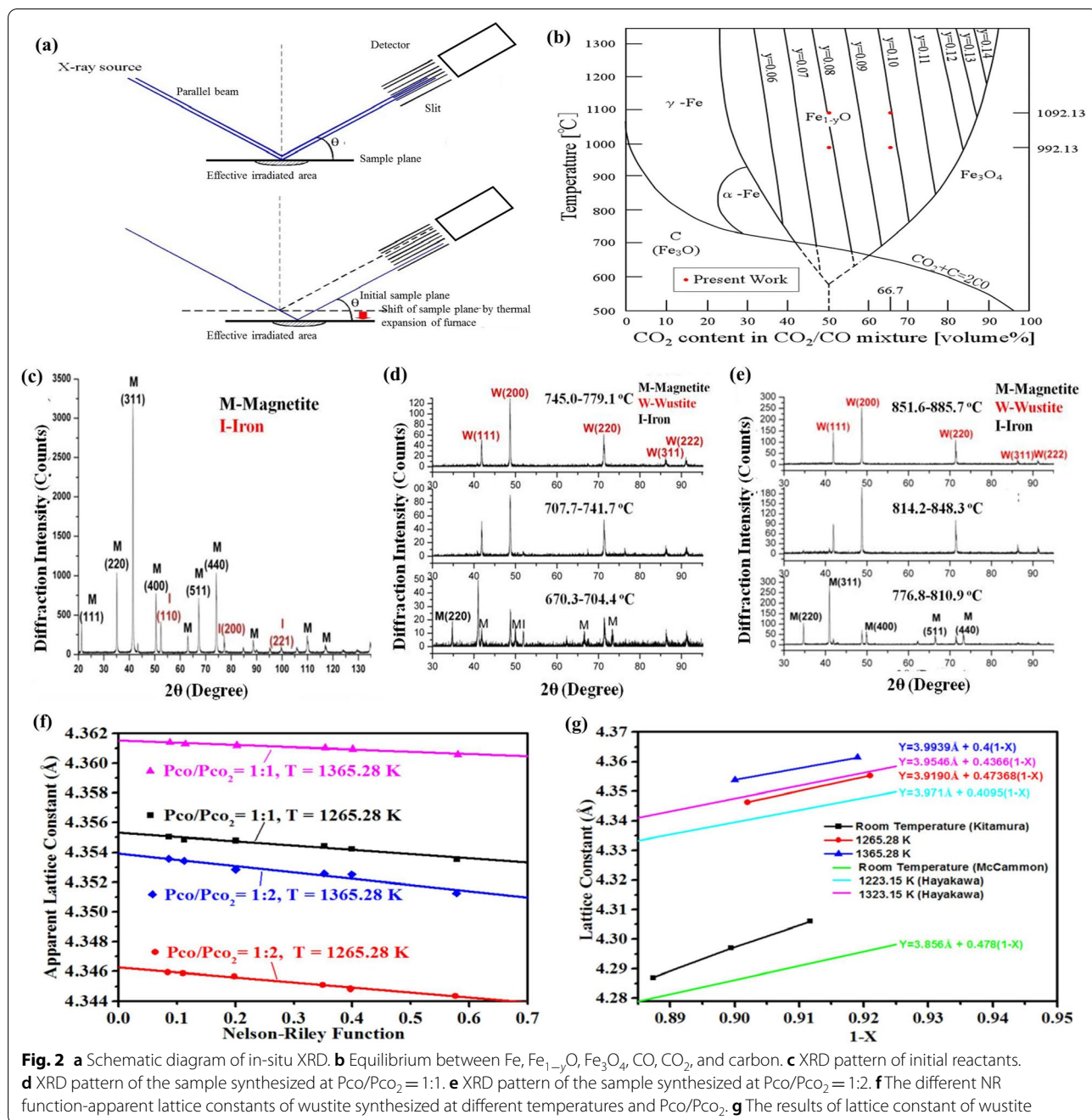
Lv *et al. Nanoscale Res Lett*   (2021) 16:138

Page 4 of 19

Fig. 2 **a** Schematic diagram of in-situ XRD. **b** Equilibrium between Fe, $Fe_{1-y}O$, Fe_3O_4, CO, CO_2, and carbon. **c** XRD pattern of initial reactants. **d** XRD pattern of the sample synthesized at $Pco/Pco_2 = 1:1$. **e** XRD pattern of the sample synthesized at $Pco/Pco_2 = 1:2$. **f** The different NR function-apparent lattice constants of wustite synthesized at different temperatures and Pco/Pco_2. **g** The results of lattice constant of wustite

Table 1 Experimental conditions of the XRD measurements

Temperature (K)	Heating rate (°C min⁻¹)	Atmosphere	Parameter	Time (min)
293.15–843.15	10	Helium	–	55
843.15–1265.28 (or 1365.28)	2	CO/CO_2	Step: 0.01°, 5° min⁻¹	215 or 265
1265.28 and 1365.28	0	CO/CO_2	Step: 0.01°, 2° min⁻¹ (full scanning), 1° min⁻¹ (scanning of 8 crystal planes)	240–420

Lv *et al. Nanoscale Res Lett*   (2021) 16:138

Page 5 of 19

of 10 °C min^{-1} until the temperature of samples reached 843.15 K, which were also in He atmosphere with the flow rate of 25 ml min^{-1}. Then, the He gas was exhausted, and CO/CO_2 gas with certain ratio (e.g., 1:1 and 1:2) was purged into the furnace. After the calibration of high temperature by melting Au flakes, the actual temperature of the sample holder could be obtained. From 843.15 K to the desired temperature (1265.28 and 1365.28 K), the heating rate was 2 °C min^{-1} and the XRD was employed to measure the sample for confirmation of the wustite phase. When the sample was reserved at the desired temperature and most of which was wustite phase, the diffraction angles of wustite's crystal planes were measured during a period of 240–420 min, then the temperature of sample raised for 50 °C and remained at this temperature for 60 min. After these procedures, the temperature of sample decreased to the former desired temperature and the XRD measurement for diffraction angles of crystal planes of wustite was conducted again in a period of 180–240 min.

The lattice constant can be obtained from a linear extrapolating of the apparent lattice constants to zero of this function, that is, 2 Theta = 180°. The diffraction peaks of (111), (200), (220), (311), and (222) crystal planes of wustite are indexed in Fig. 2d, e, and the XRD pattern of the sample is obtained at P_{CO}/P_{CO_2} of 1:1 and 1:2, respectively. The relation between apparent lattice constant and Nelson–Riley function under different P_{CO}/P_{CO_2} and temperatures is obtained, as shown in Fig. 2f. The straight lines represent the squares fitting to the data. By means of these straight lines, the apparent lattice constants were extrapolated to the zero of Nelson–Riley function. Therefore, as shown in Fig. 2f: the results of the true lattice constants obtained at different temperatures and P_{CO}/P_{CO_2} are 4.355 Å (1265.28 K, P_{CO}/P_{CO_2} = 1:1), 4.346 Å (1265.28 K, P_{CO}/P_{CO_2} = 1:2), 4.362 Å (1365.28 K, P_{CO}/P_{CO_2} = 1:1) and 4.354 Å (1365.28 K, P_{CO}/P_{CO_2} = 1:2), respectively. As shown in Fig. 2g, the lattice constant increases with the increase of x of $Fe_{1-x}O$, and the higher the temperature, the larger the lattice constant. The relation between the composition and lattice constant of wustite at high temperature can be obtained as following Eqs. (3) and (4).

$$a\left(Å\right) = 3.919 + 0.474(1 - x)(1265.28\ \text{K}) \quad (3)$$

$$a\left(Å\right) = 3.994 + 0.400(1 - x)(1365.28\ \text{K}) \quad (4)$$

^{57}*Fe Mössbauer Spectroscopy*

The ^{57}Fe Mössbauer spectroscopy involves properties of the nucleus, including energy level structure of the nucleus and the chemical environment in which the nucleus is located. Hence, it can be applied accordingly to study the valence of atoms, the ionicity of chemical bonds, coordination number, crystal structure, electron density and magnetic properties of sample. The ^{57}Fe Mössbauer spectroscopy is widely utilized in the fields of chemistry and materials. Herein, we elaborate the ^{57}Fe Mössbauer spectroscopy for characterizing iron oxides. The ^{57}Fe Mössbauer spectroscopy is used to distinguish and characterize various iron oxide phases, and to monitor the local environment of Fe atoms in crystal lattice [39, 40].
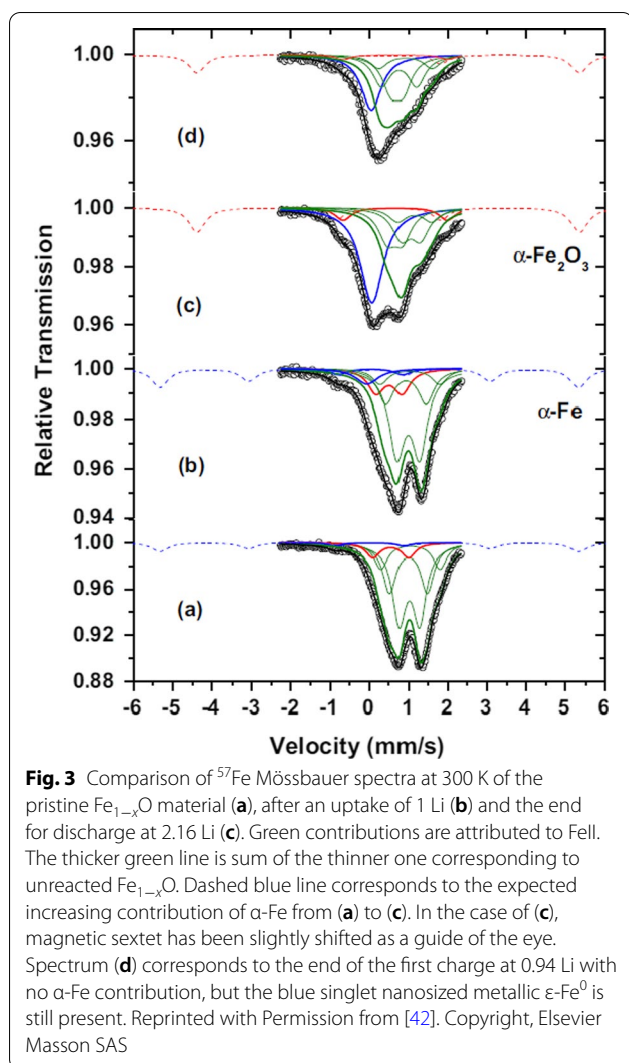
The hyperfine parameters, such as isomer shift (IS), quadrupole splitting (QS), quadrupole shift (ε_Q) and hyperfine magnetic field (B_{hf}) can be obtained by analyzing the position of the spectral lines in Mössbauer spectrum [41, 42]. The characteristics of the sample can be inferred from the width and asymmetry of the spectral lines. Through temperature and field dependence of the hyperfine parameters also allows deducing valuable parameters.

Aldon et al. [42] studied lithium-induced conversion reaction of $Fe_{1-x}O$ using ^{57}Fe Mössbauer spectroscopy. The hyperfine parameters (IS and QS) are rather characteristic of FeII species in antiferromagnetic (TN = 198 K [43]) $Fe_{1-x}O$, showing a typical paramagnetic absorption at room temperature (RT). As indicated in the ^{57}Fe Mössbauer spectrum (Fig. 3a), there are three broadened doublets with an IS ~ 1 mm s^{-1} and QS ranging from ~ 0.50 to 1.50 mm s^{-1}, and their relative areas are corrected from α-Fe magnetic contribution. The absorption intensities are 42, 26 and 15%. A fourth doublet centered at IS ~ 0.55 mm s^{-1}, QS ~ 0.90 mm s^{-1} with a relative area of 11% is common for FeII^I species, as expected in non-stoichiometric $Fe_{1-x}O$. From the FeII/FeII^I ratio, the amount of vacancies is estimated as ~ 0.057 ± 0.008, closed to 0.050 by XRD characterization. Finally, the doublet located at QS ~ 1.68 mm s^{-1} and IS ~ 0 mm s^{-1}, corresponding to α-Fe, makes a contribution of ~ 6%.

Comparing with Fe_2O_3 and Fe_3O_4, the specific capacity of $Fe_{1-x}O$ is lowest. Besides, its synthesis method is more complicated. In most cases, the reduction reaction at high temperature is inevitable [3–6, 9, 11]. As a result, $Fe_{1-x}O$ is not an ideal LIBs anode comparing with Fe_2O_3 or Fe_3O_4.

Fe_2O_3 Based Nanostructures

Among these iron oxides, especially Fe_2O_3, is attracting many researchers' attention due to the high theoretical capacity, which can reach 1000 mA h g^{-1} [44]. Additionally, Fe_2O_3 has distinctive advantages, such as high resistance to corrosion, low production cost, environmental friendliness, nonflammability, nontoxicity and high natural availability [45]. Due to these excellent properties,

Lv *et al. Nanoscale Res Lett*   (2021) 16:138

Page 6 of 19

Fig. 3 Comparison of ^{57}Fe Mössbauer spectra at 300 K of the pristine $Fe_{1-x}O$ material (**a**), after an uptake of 1 Li (**b**) and the end for discharge at 2.16 Li (**c**). Green contributions are attributed to FeII. The thicker green line is sum of the thinner one corresponding to unreacted $Fe_{1-x}O$. Dashed blue line corresponds to the expected increasing contribution of α-Fe from (**a**) to (**c**). In the case of (**c**), magnetic sextet has been slightly shifted as a guide of the eye. Spectrum (**d**) corresponds to the end of the first charge at 0.94 Li with no α-Fe contribution, but the blue singlet nanosized metallic ε-Fe^0 is still present. Reprinted with Permission from [42]. Copyright, Elsevier Masson SAS

Fe_2O_3 is highly promising for applications in LIBs anode [46–50]. Herein, a concise overview of recent development about the synthesis, characterization and electrochemical performance of Fe_2O_3 based nanostructures is provided.

Synthesis and Characterization
In last decade, there are enormous efforts for exploring synthetic methods of Fe_2O_3 based nanostructures. In this section, we elaborated and summarized synthetic methods of Fe_2O_3 based nanostructures, including gas phase deposition [51], solution based method [52], electrochemical method [53], thermal treatment [54] and other methods [55, 56]. Also, we compared different synthesis methods.

Additionally, the ^{57}Fe Mössbauer spectroscopy characterization of Fe_2O_3 nanostructures is described in details. Since only certain nuclei has resonance absorption, the

^{57}Fe Mössbauer spectroscopy is not interfered by other elements. The range of the ^{57}Fe Mössbauer spectroscopy affected by extranuclear environment is generally within several nanometers, so it is very suitable for characterizing nanostructure.

Gas Phase Deposition
Gas phase deposition is widely applied in synthesis of many thin films and other nanostructures, such as Fe_2O_3 and other iron oxides based nanostructures. Chemical vapor deposition (CVD), atomic layer deposition (ALD), physical vapor deposition (PVD), electrolytic deposition and reactive sputtering are typical methods of gas phase deposition [57–60].

ALD is a unique way to synthesize high-crystallinity thin films, and a cheaper route than liquid phase deposition. In ALD process, the chemical reaction of every layer is directly accompanied with the former layer. In this way, only one layer is deposited per reaction cycle. For instance, Lin et al. [51] utilized ALD to deposit a high-quality ultrathin α-Fe_2O_3 film on $TiSi_2$ nanonets. The 3D self-organized nanoporous thin films were fabricated by Yang et al. [61] through CVD and integrated into a heterogeneous Fe_2O_3/Fe_3C-graphene. As LIBs anode, it's rate capacity and cyclability can be greatly improved by deposition of this thin film. Cesar et al. [62] deposited thin films of silicon-doped Fe_2O_3 dendritic nanostructures by atmospheric pressure CVD (APCVD), which produced Fe_2O_3 photoanodes that oxidize water under visible light with unprecedented efficiency. The dendritic α-Fe_2O_3 nanostructures showed a macroscopic surface area of 0.5 cm^2 [62]. The vertically aligned α-Fe_2O_3 nanorods array is grown on a silicon substrate via metal–organic CVD (MOCVD) by Wu et al. [63]. What's more, Jia et al. [64] utilized a radio frequency sputtering deposition to fabricate α-Fe_2O_3 ultrathin films.

Although gas phase deposition is capable of preparing high-quality Fe_2O_3 based nanostructures, it also has disadvantages. For example, APCVD and MOCVD have high toxicity and flammability in the process of precursors.

Solution Based Synthetic Method
The solution based synthetic method is common and facile to fabricate Fe_2O_3 and other iron oxides. Fe_2O_3 with various morphologies, such as nanoflowers [65], nanospheres [66], nanoparticles [67], nanorods [68], nanotubes [14], nanorings [69], nanobelts [70], nanoflakes [71], nanowires [72], nanofibers [73], and microboxes [54], were synthesized by solution based method, e.g., hydrothermal, solvothermal and sol–gel approaches. These methods are highly facile and available. Zhong et al. [65] used a solvothermal method to fabricate Fe_2O_3

Lv *et al. Nanoscale Res Lett* (2021) 16:138

Page 7 of 19

nanoflowers (Fig. 4) via an ethylene glycol-mediated self-assembly process. Vayssieres et al. [52] reported the growth of porous Fe_2O_3 nanorods array on fluorine doped tin oxide (FTO) conducting glass by a hydrothermal process. By hydrothermal growth of α-Fe_2O_3 precursor on SnO_2 nanowire stems, a novel six-fold-symmetry branched α-Fe_2O_3/SnO_2 heterostructure (Fig. 5) was synthesized [74]. There is another facile and economical technique, sol–gel method, for synthesizing Fe_2O_3 nanostructures. Woo et al. [68] utilized a sol–gel method to obtain α-Fe_2O_3 nanorods by reaction of ubiquitous Fe^{3+} in reverse micelles. The nanorods obtained by this mechanism have low dimensionality and high surface area, which can be extended to magnetite and wustite.

Electrochemical Method

Electrochemical method is utilized to synthesize Fe_2O_3 nanostructures, e.g., the electrochemical deposition is applied in fabricating Fe_2O_3 nanoparticles [53]. Through anodization of iron foil in ethylene glycol electrolyte solution containing deionized (DI) water and NH_4F at a voltage of 30–60 V, α-Fe_2O_3 nanotubes array was obtained [75]. In addition, electrochemical anodization is employed to synthesize Fe_2O_3 nanotubes array [76]. Mao et al. [77] reported the synthesis of Fe_2O_3 array using electrochemical deposition. In their research work, iron was deposited into AAO template channels by electrochemical deposition, then the AAO template was removed by NaOH solution, and finally the iron nanorods array was converted to Fe_2O_3 array. The characteristic of this research is that, by changing the duration of deposition, the length of Fe_2O_3 nanorods can be finely controlled.
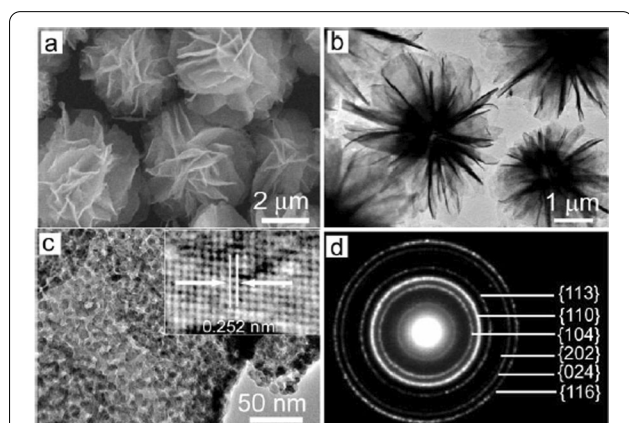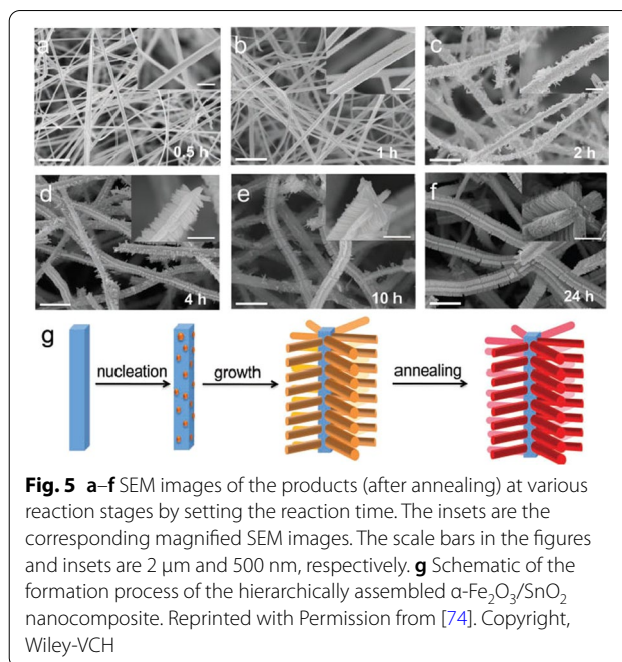

Fig. 5 **a–f** SEM images of the products (after annealing) at various reaction stages by setting the reaction time. The insets are the corresponding magnified SEM images. The scale bars in the figures and insets are 2 μm and 500 nm, respectively. **g** Schematic of the formation process of the hierarchically assembled α-Fe_2O_3/SnO_2 nanocomposite. Reprinted with Permission from [74]. Copyright, Wiley-VCH

Thermal Treatment

The thermal treatment for synthesizing Fe_2O_3 involves two significant approaches, thermal oxidation and thermal pyrolysis. For example, Zhang et al. [54] prepared Fe_2O_3 microboxes (Fig. 6) via thermally induced oxidative decomposition of prussian blue (PB) microcubes at 350–650 °C. The solid-state approach will provide a more facile way for large-scale synthesis of uniform anisotropic hollow structures in comparison with the widely used solution based method. Fe_2O_3 with different morphologies were prepared via commanding thermal oxidation
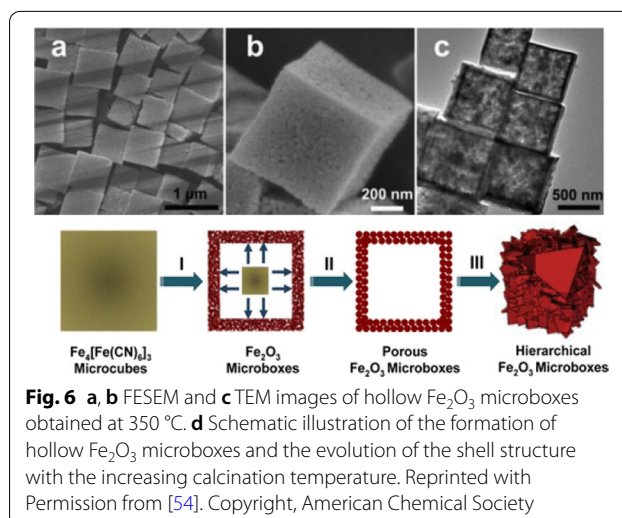

Fig. 4 **a** SEM and **b** TEM images of the as-obtained α-Fe_2O_3. **c** High-magnification TEM image of the petal of the flowerlike structure of the as-obtained α-Fe_2O_3. **d** SAED pattern of the obtained α-Fe_2O_3. Reprinted with Permission from [65]. Copyright, Wiley-VCH

Fig. 6 **a**, **b** FESEM and **c** TEM images of hollow Fe_2O_3 microboxes obtained at 350 °C. **d** Schematic illustration of the formation of hollow Fe_2O_3 microboxes and the evolution of the shell structure with the increasing calcination temperature. Reprinted with Permission from [54]. Copyright, American Chemical Society

Lv *et al. Nanoscale Res Lett*   (2021) 16:138

Page 8 of 19

parameters. α-Fe$_2$O$_3$ nanostructures by facile thermal treatment of iron based precursors are proposed. For instance, Rao and Zheng [71] utilized heat treatment to prepare densely aligned α-Fe$_2$O$_3$ nanoflakes array.

Thermal pyrolysis is another common method to deposit Fe$_2$O$_3$ thin films. Duret et al. [78] applied this method to obtain mesoscopic α-Fe$_2$O$_3$ leaflet films through ultrasonic spray pyrolysis, while the fabricated films have higher photoactivity than those fabricated by conventional spray pyrolysis techniques. Also, the synthesis of α-Fe$_2$O$_3$ nanoflakes, nanoflowers, nanowires and nanorods array via vapor phase deposition, liquid phase deposition and thermal treatment is reported [63, 71, 72, 79].

Other Methods

In 2016, Guivar et al. [55] compounded vacancy ordered maghemite (γ-Fe$_2$O$_3$) nanoparticles functionalized with nanohydroxyapatite (nanoHAp), using a typical co-precipitation chemical route. Remarkably, the γ-Fe$_2$O$_3$ functionalized with nanoHAp labeled as γ-Fe$_2$O$_3$@HAp is formed without any thermal process as calcination.

There are many ways to synthesize Fe$_2$O$_3$, but most of them are not environmentally friendly. In 2019, Bashir et al. [56] developed an eco-friendly method to obtain α-Fe$_2$O$_3$ nanoparticles, using Persea Americana seeds extract. They used two different precursors to prepare two samples of α-Fe$_2$O$_3$, one sample (A) prepared from Fe(NO$_3$)$_3$·9H$_2$O, and another sample (B) prepared FeCl$_3$·9H$_2$O.

The ^{57}Fe Mössbauer spectra of samples A and B recorded at 300 K (room temperature (RT)) are presented in Fig. 7. The ^{57}Fe Mössbauer spectroscopy is a very valuable technique for exploring the local magnetic behavior and oxidation state of iron atoms in a particular matrix [80]. Both samples revealed magnetic ordering, and displayed only single sextet indicating magnetically ordered state. Table 2 shows ^{57}Fe extracted Mössbauer parameters at RT, which lists IS, ε_Q and B_{hf}. Both samples' B_{hf} above 51 T are related to α-Fe$_2$O$_3$ [81]. Furthermore, the values of ε_Q is also consistent with α-Fe$_2$O$_3$. Both quadrupole interactions indicate Fe as Fe^{3+} since the observed IS of 0.3653 mm/s and 0.3754 mm/s for the samples A and B, respectively, are typical for Fe^{3+} [82]. Therefore, the negative values of quadrupole splitting indicate the weak ferromagnetic property of the samples A and B, the characteristic of pure α-Fe$_2$O$_3$ phase.

Electrochemical Performance

The charge/discharge cycling at the voltage window of 0.005–3.0 V (vs. Li$^+$) under a current density of 200 mA g^{-1} at RT is shown in Fig. 8a. During the initial discharge process, there is an obvious voltage platform
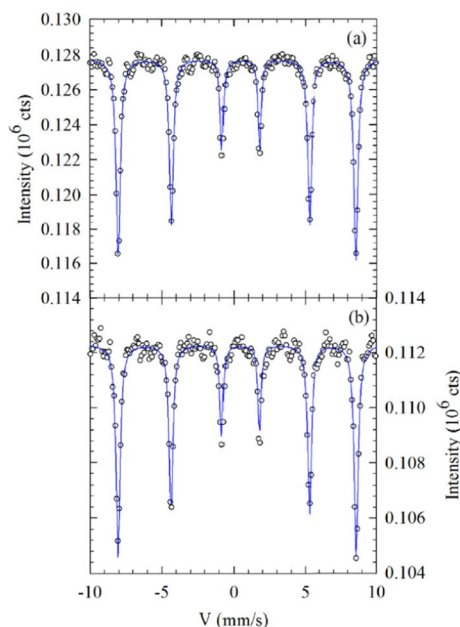

Fig. 7 ^{57}Fe Mössbauer spectra recorded at room temperature for α-Fe$_2$O$_3$ nanoparticles. **a** sample A (ferric nitrate as a precursor) and **b** sample B (ferric chloride as a precursor). Reprinted with Permission from [56]. Copyright, American Chemical Society

Table 2 Mössbauer parameters IS, (ε_Q), B_{hf} and relative area for samples A and B (Reprinted with Permission from [56]. Copyright, American Chemical Society.)

Sample	IS (mm s^{-1})	ε_Q (mm s^{-1})	B_{hf} (T)	Relative area (%)
A	0.36 (1)	− 0.095 (1)	51.6 (4)	100
B	0.37 (1)	− 0.11 (1)	51.4 (3)	100

of ∼ 0.75 V, and it gradually moved to a voltage plateau of ∼ 1.0 V, and remain stable in the second and fifth cycles. Meanwhile, an ambiguous plateau was observed at ∼ 1.8 V in the charge process. The first discharge profile qualitatively resembles the results by Larcher et al. [83] and Morales et al. [84] on nanoparticle Fe$_2$O$_3$, and Wang et al. [14] on Fe$_2$O$_3$ nanotubes. The cycling performance of three samples (hierarchical Fe$_2$O$_3$ microboxes, Fe$_2$O$_3$ microboxes and porous Fe$_2$O$_3$ microboxes) is discribed in Fig. 8b. After 30 cycles, hierarchical Fe$_2$O$_3$ microboxes exhibit the highest reversible capacity of 945 mA h g^{-1}, follow by 872 mA h g^{-1} for porous Fe$_2$O$_3$ microboxes, and finally 802 mA h g^{-1} for Fe$_2$O$_3$ microboxes. The results demonstrated that three samples display excellent cycling stability, and the morphology of nanostructured Fe$_2$O$_3$ plays a significant role in determining the discharge characteristics.
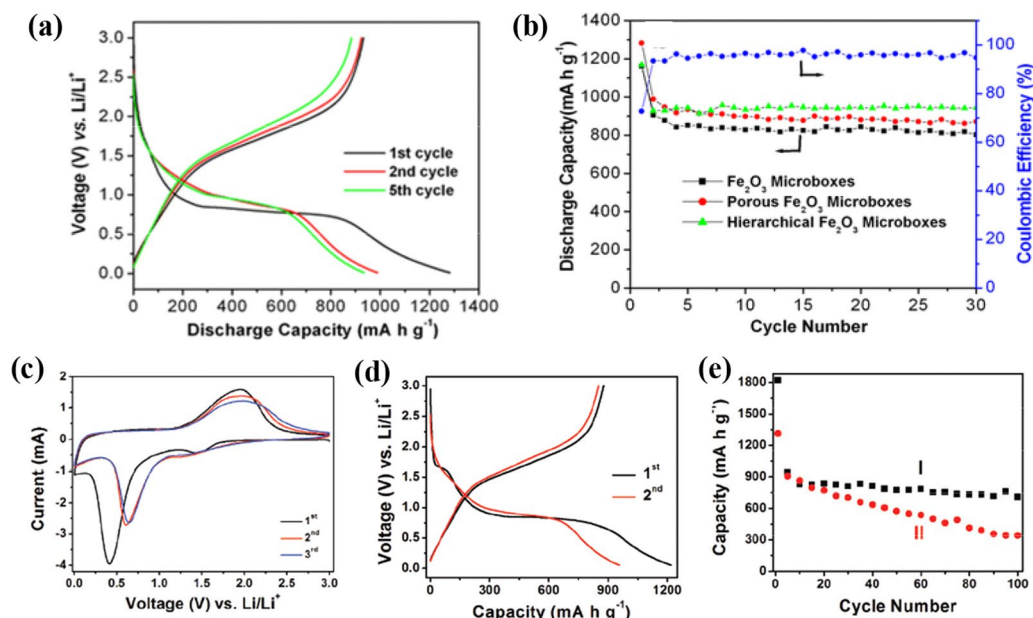
Lv et al. Nanoscale Res Lett   (2021) 16:138

Page 9 of 19

Fig. 8 a Discharge — charge voltage profiles of porous Fe_2O_3 microboxes obtained at 550 °C. **b** Cycling performance of Fe_2O_3 microboxes (350 °C), porous Fe_2O_3 microboxes (550 °C), and hierarchical Fe_2O_3 microboxes (650 °C) and Coulombic efficiency of porous Fe_2O_3 microboxes (550 °C) over the voltage range $0.01 - 3.0$ V vs. Li/Li^+ at the same current density of 200 mA g^{-1}. (**a**, **b** Reprinted with Permission from [54]. Copyright, American Chemical Society). Electrochemical measurements of the sample. **c** CVs between 5 mV and 3 V at a scan rate of 0.5 mV s^{-1}. **d** Charge–discharge voltage profiles. **e** Comparative cycling performance of (I) the as-prepared α-Fe_2O_3 hollow spheres and (II) α-Fe_2O_3 microparticles. All the galvanostatic tests are performed at a constant current rate of 200 mA g^{-1} between 0.05 and 3 V. **c–e** Reprinted with Permission from [85]. Copyright, American Chemical Society

Cyclic voltammogram (CV) is used to characterize the cells with α-Fe_2O_3 nanoflakes anode in the 0.005–3.0 V under a slow scan rate (at RT). Li metal is used as the counter and reference electrodes [20], consistent with previously reported results [85]. CV curves of α-Fe_2O_3 hollow spheres between 5 mV and 3 V at a scan rate of 5 mV s^{-1} are presented in Fig. 8c. There are apparent redox current peaks, and demonstrate good reversibility of electrochemical reaction. As shown in Fig. 8d, a distinct voltage plateau can be discovered at ~ 0.75 V, consistent with CV curves. The charge–discharge voltage profiles reflect the lithium storage capacity of α-Fe_2O_3. The first cyclic discharge capacity and the charge capacity is 1219 mA h g^{-1} and 877 mA h g^{-1} respectively, which lead to a relatively low irreversible capacity loss of 28%. In the second cycle, the Coulombic efficiency increased quickly to 89%. Cycling performance of two samples are demonstrated in Fig. 8e. The sample (I) exhibits excellent cyclic capacity retention from the second cycle onward. After 100 cycles of charge/discharge, the reversible capacity is still as high as 710 mA h g^{-1}. Compared with α-Fe_2O_3 microparticles, the unique hierarchical α-Fe_2O_3 hollow spheres apparently have enhanced Li storage performance, and

a more stable cycling capacity retention and a higher reversible capacity are realized. This superior performance can be attributed to the thin nanosheet subunits that provide rapid and efficient transport of Li^+, as well as the unique hollow interior that allows the material to effectively buffer the stress generated during charge/discharge process.

Iron oxides are cheap, abundant and environmentally compatible, and Fe_2O_3 has excellent electrochemical performance. Some of the above studies have shown that Fe_2O_3 based nanostructures can be an alternative anode to replace the presently used graphite in LIBs. The nanostructured Fe_2O_3 has great potential in LIBs anode [86–95]. Recently, several studies about Fe_2O_3 anode in asymmetric supercapacitors are reported [96–100]. However, low surface area and poor electrical conductivity are still two critical issues limiting the specific capacitance and power density of Fe_2O_3. For solutions of these problems, CNTs and CNFs are regarded as conductive matrices to load Fe_2O_3 nanoparticles for realizing improved performance [101]. Table 3 summarizes some typical Fe_2O_3 based nanostructures with their synthesis and electrochemical performance.

Lv *et al. Nanoscale Res Lett*   (2021) 16:138

Page 10 of 19

Table 3 A summary of electrochemical performance of Fe_2O_3 based nanostructures

Active electrode	Synthesis	Electrochemical performance	References
Single-crystalline α -Fe_2O_3 nanosheets on conductive substrates	Thermal heating	700 mA h g^{-1} after 80 cycles at 65 mA g^{-1}	[20]
Uniform single-crystalline α-Fe_2O_3 nanodiscs	Controlled oxalic acid etching process	662 mA h g^{-1} after 100 cycles at 200 mA g^{-1}	[102]
Single-crystalline α-Fe_2O_3 nanosheets grown directly on Ni foam	Template-free growth	518 mA h g^{-1} after 50 cycles at 0.1 C	[103]
Hierarchical α-Fe_2O_3 hollow spheres with sheet-like subunits	Quasimicroemulsion-templated hydrothermal reaction	710 mA h g^{-1} after 100 cycles at 200 mA g^{-1}	[85]
Hierarchical Fe_2O_3 microboxes	Annealing prussian blue (PB) microcubes	945 mA h g^{-1} after 30 cycles at 200 mA g^{-1}	[54]
Carbon-coated α-Fe_2O_3 hollow nanohorns grafted on CNT backbones	Direct growth and thermal transformation of β-FeOOH nanospindles on CNTs, followed by carbon nano-coating	800 mA h g^{-1} after 100 cycles at 500 mA g^{-1}	[104]
α-Fe_2O_3 nanowires	Low-temperature CVD	456 mA h g^{-1} after 100 cycles at 0.1 C	[105]

Fe_3O_4 Based Nanostructures

Magnetite (Fe_3O_4) and Fe_3O_4 based nanostructure composites with pseudocapacitance, high theoretical capacity, environmental friendliness and low cost, are extensively applied to electromagnetic wave absorption [106], LIBs [3, 12, 15], biotechnological devices [107, 108], and supercapacitor [4, 109]. Fe_3O_4 nanoparticles is one of the high-performance anodes in electrochemical devices. Unfortunately, Fe_3O_4 nanostructures still face some problems, such as a severe volume variation (~200%) during the insertion and extraction of Li^+ and relatively low electrical conductivity, posing negative influence on the cycling stability [19, 110, 111]. From research results, we found that the structure and morphology of Fe_3O_4 have a high influence on the electrochemical performance of Fe_3O_4 and Fe_3O_4 based composites.

Synthesis and Characterization

Recently, nanostructure engineering is demonstrated as a highly-effective approach to obtain improved electrochemical performance of Fe_3O_4 and Fe_3O_4 based composites. Therefore, various nanostructures including 0D nanoparticles [112], 1D nanorods/wires [113, 114], 2D nanoflakes/sheets [115, 116], 3D hierarchical/porous architectures [117, 118], and hybrid nanostructures of iron oxides [16] are proposed. The electrochemical performance of Fe_3O_4 nanostructures can be optimized by rational design of their morphology, composition, porosity and surface characteristics.

Solution phase synthetic method is a facile and rapid way to obtain Fe_3O_4 based nanostructures, because of the associative advantages, such as low synthesis temperature (always below 250 °C), easy control of morphology via adjusting hydrothermal conditions (e.g., PH, density of reactant and dosage of active agent, etc.). Solution phase synthetic method includes solvothermal synthesis

[119], thermolysis [120], co-precipitation [121], sol–gel process [122, 123], micro-emulsion [124], etc. Simultaneously we compare the pros and cons of these methods.

Solvothermal Synthesis

Solvothermal synthesis, which reacts in a special closed reaction vessel, is one commonly used methods for synthesizing Fe_3O_4. In a hermetic environment, it is a facile method using aqueous solution as reaction medium at high temperature and high-pressure hermetic environment. Fe_3O_4 nanostructures with various morphologies (0D, 1D, 2D and 3D) were synthesized applying this approach.

An et al. [119] obtained the Fe_3O_4/graphene nanowires by solvothermal synthesis and calcination with $FeCl_3$, NH_4VO_3 and graphene as precursors. Phase transition of Fe_3O_4/VO_x (FVO) after annealing was confirmed by XRD. For the XRD pattern of sample without annealing, all diffraction peaks of FVO and graphene decorated FVO correspond to $FeVO_4 \cdot 1.1H_2O$. For the XRD pattern of sample after annealing, there are no peaks of any vanadium oxides. And the inductive coupled high frequency plasma (ICP) result indicated that the molarity ratio of Fe and V is ~0.94:1, confirming the existence of amorphous vanadium oxide.

Mu et al. [125] reported dispersed Fe_3O_4 nanosheets on carbon nanofiber by combing the electrospinning and solvothermal process. In this work, Fe_3O_4 nanosheets are uniformly attached on the surface of carbon nanofiber with the diameter of about 500 nm.

Fe_3O_4 nanoparticle with high specific surface area via $FeCl_3$ and organic solvent ethanolamine (ETA) as precursors is reported by Wang et al. [126]. In this preparation, ETA is critical factor for compounding Fe_3O_4 nanoparticles with high specific surface area, and Fe^{3+} is gradually reduced to Fe^{2+} by ETA during dissolution process,

Lv *et al. Nanoscale Res Lett*   (2021) 16:138

Page 11 of 19

demonstrating that Fe^{2+} increased as the increase of ultrasonication time. The ratio of ETA and $FeCl_3$ has a large impact on the nanoscale grain size and specific surface area of Fe_3O_4. And the results showed that the grain size of 20–40 nm is achieved with 60 mL ETA and 6 mmol $FeCl_3$. When the amount of ETA is 80 mL, smaller nanoparticles (5–10 nm) are obtained.

Another representative work is reported by Chen et al. [127], in which graphene nanosheets decorated with Fe_3O_4 nanoparticles (USIO/G) were synthesized using a facile solvothermal process. For the synthesis of USIO composite decorated with reduced graphene oxide (RGO), is used $FeCl_3 \cdot H_2O$ as precursor, then $NaHCO_3$ and L-ascorbic acid were added to form USIO/G. In this process, L-ascorbic acid was oxidized to dehydroascorbic acid (DHAA) by some of Fe^{3+}, which were reduced to Fe^{2+}. Formation process of USIO/G is schematically shown in Fig. 9. The Fe_3O_4 nanoparticles with uniform distribution, which are beneficial for electrical conductivity of graphene, mitigation of volume expansion of Fe_3O_4, and facilitating Fe_3O_4 particles into the electrolyte.

Xiong et al. [128] a kind of hierarchical hollow Fe_3O_4 (H-Fe_3O_4) microspheres prepared by controlled thermal decomposition of iron alkoxide precursor. In a classical reaction, ethylene glycol (EG) serves as reduction reagent that partly reduces Fe^{3+} to Fe^{2+} with sodium acetate (NaAc), and polyvinylpyrrolidone (PVP) [128]. For this synthesis, PVP served as a surface stabilizer, which has important role in the formation and transformation of hollow interiors.
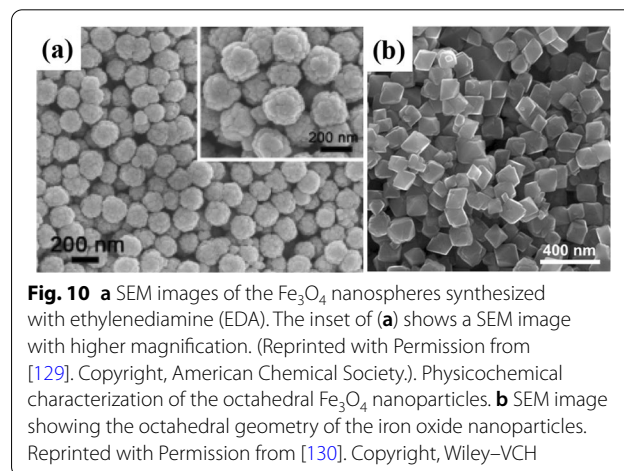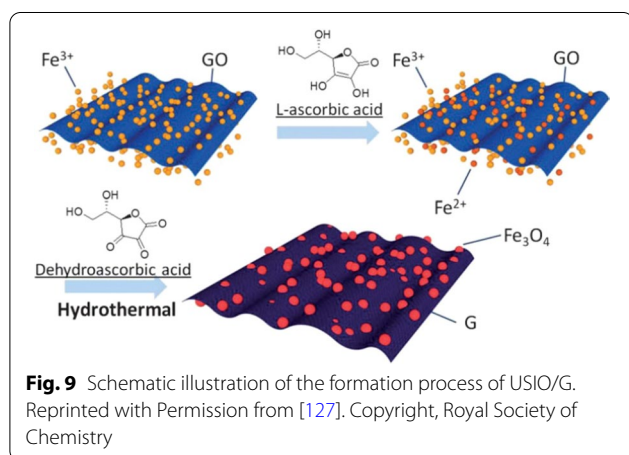
With the development of solvothermal synthesis, it emerging as an efficient method with the advantages of low energy consumption, little reunion and easy to control shape, etc. Chen et al. [129] synthesized poly (acrylic acid) (PAA)-entangled Fe_3O_4 nanospheres by a facile solvothermal method. In their synthesis, the ethylenediamine is crucial to the controlling of the uniformity of nanospheres, and the PAA molecules served as carbon source that transforms into the carbon matrix by heating treatment in inert atmosphere. As shown in SEM image of the prepared C-Fe_3O_4 nanospheres, very uniform spherical particles with a diameter of 150–200 nm are synthesized. Observed from SEM images in Fig. 10a, the nanospheres contain small irregular particles, and have a relatively rough surface. In the control experiment without ethylenediamine (EDA), the synthesized particles are much less uniform with a wider size distribution of 100–500 nm, allowing the formation of nanospheres with smaller size.

Co-precipitation

Due to its high cost-effectiveness, environmental friendliness, and facile synthesizing protocol, co-precipitation is a general approach for Fe_3O_4 nanoparticles. Thus, in iron based rechargeable battery systems, Fe_3O_4 nanomaterials are especially suitable for large-scale electrochemical applications to solve the energy requirement of the modern society.

Li et al. [121] proposed Fe_3O_4 polyhedron as LIBs anode for alkaline secondary batteries by a co-precipitation. Annealing temperature makes a high effect on the physical and electrochemical performance of Fe_3O_4 nanomaterials. The 700 °C-annealed Fe_3O_4 exhibited a higher electrochemical performance, such as a higher specific discharge capacity of 604.2 mA h g^{-1} with a charging efficiency of 83.9% at 120 mA g^{-1}. Ooi et al. [130] demonstrated octahedral Fe_3O_4 nanoparticles using a facile solvothermal route. Scanning electron microscope (SEM) image of Fe_3O_4 nanoparticles is shown in Fig. 10b, which depicts that octahedral Fe_3O_4 nanoparticles with an average length of 93 ± 18 nm were prepared by the hydrothermal method, showing a roughly

Fig. 9 Schematic illustration of the formation process of USIO/G. Reprinted with Permission from [127]. Copyright, Royal Society of Chemistry

Fig. 10 a SEM images of the Fe_3O_4 nanospheres synthesized with ethylenediamine (EDA). The inset of (**a**) shows a SEM image with higher magnification. (Reprinted with Permission from [129]. Copyright, American Chemical Society.). Physicochemical characterization of the octahedral Fe_3O_4 nanoparticles. **b** SEM image showing the octahedral geometry of the iron oxide nanoparticles. Reprinted with Permission from [130]. Copyright, Wiley–VCH

Lv *et al. Nanoscale Res Lett*   (2021) 16:138

Page 12 of 19

Gaussian size distribution. Then, the crystal structure of octahedral nanoparticles can be further evaluated by HRTEM, and the composition of the bulk sample was further characterized by XRD and X-ray photo electron spectroscopy (XPS).

Thermolysis

The thermolysis is small monodisperse magnetic nanocrystals synthesized by organic metal compounds in high boiling point solvents containing stabilizing agent. Previous Organic metal bodies include metal acetylacetone compounds, metal cupferron, or metal Carbonyl compounds, and usually choose fatty acids, oleic acid, or hexadecyl amine as a surfactant. Zhang et al. [120] reported ultrafine Fe_3O_4 nanocrystals uniformly encapsulated in two-dimensional (2D) carbon nanonetworks through thermolysis of $Fe(C_5H_7O_2)_3$ precursor at 350 °C under vacuum, which named as 2D Fe_3O_4/C nanonetworks. This facile process using low-cost precursor proposed a green approach for preparing Fe_3O_4/carbon composite. Additionally, compared with the reported Fe_3O_4/carbon composites, the particle size of Fe_3O_4 is controllable and a size of ~ 3 nm can be obtained.

Benefitting from synergistic effects of carbon nanonetworks with excellent electrical conductivity and ultrafine Fe_3O_4 particles with uniform distribution, high reversible capacity, excellent rate capability and superior cyclability at the voltage of 0.01–3.0 V (vs. Li/Li$^+$) are obtained. Nanoparticles with unique iron oxide (Fe_3O_4) cores and zinc oxide (ZnO) shells were prepared by Jaramillo et al. [131]. Fe_3O_4 nanoparticle synthesized through a thermolysis method using $Fe(C_5H_7O_2)_3$ as organic metal body presoma, triethylene glycol as surface active agent, and core–shell Fe_3O_4@ZnO nanoparticles were successfully synthesized using straightforward methodologies. The structural and optical properties of the materials were characterized using a combination of X-ray diffraction, electron microscopy, and light spectroscopy. Importantly, the purity of the core and shell phases in the Fe_3O_4@ZnO nanoparticles was confirmed by both XRD and TEM, and the ZnO shell was shown to increase the transparency of the core–shell nanoparticles relative to the single-component Fe_3O_4 nanoparticles. Zhang et al. [132] demonstrated a high crystalline Fe_3O_4-graphene composite by one-step reaction of thermolysis. And they demonstrated that the attachment of iron-organic complex with graphene oxide (GO) sheets can facilely result in magnetic graphene composites via a time-dependent calcination process.

Sol–Gel Process

The specific method is using the metal alkoxide, metal mineral compound or a mixture of the above two substances to hydrolysis and polymerization, uniform gel gradually, then condense into a transparent gel, however, after drying and heating, finally the oxide ultrafine powders was received. Tang et al. [122] prepared nanostructured magnetite thin film by sol–gel method using inexpensive iron (II) chloride precursor. Fe_3O_4 nanoparticles were prepared at 300 °C, however, α-Fe_2O_3 is generated when temperature increased to 350 °C, and this result restricts its applications. Xu et al. [123] proposed magnetite nanoparticles by virtue of sol–gel process combined with annealing in vacuum at 200–400 °C using nontoxic and low-cost ferric nitrate. In their study, Fe_3O_4 nanoparticles with various sizes can be synthesized facilely through varying the annealing temperature.

Micro-emulsion Method

Micro-emulsion is composed of two mutual miscibility of liquid mixture of thermodynamic stability and isotropy dispersion, one of these or two kinds of liquid called micro area, and fixed by interface layer of the surfactant molecules. The key factors controlling the reaction solution contain concentration, pH value, reaction time and temperature. Micro-emulsion as a rapid expansion of new technology possesses many advantages. For example, high purity and uniform particle size distribution molecular dopant was synthesized at low temperature and simple reaction process. But there are also some shortcomings, for instance, the reaction system mostly contains organic solvents, which leads to high cost, pollution of environmental health and long reaction time. The prepared Fe_3O_4 nanoparticles have excellent catalytic performance for the synthesis of quinoxaline in different solvents. Novel core–shell magnetic Fe_3O_4/silica nanocomposites with triblock-copolymer grafted on their surface (Fe_3O_4@SiO_2@MDN) were successfully synthesized by combining sol–gel process with seeded aqueous-phase radical copolymerization approach [133]. The Fe_3O_4@SiO_2@MDN microspheres were synthesized in following three steps. Firstly, the initial magnetic Fe_3O_4 microspheres were synthesized by a solvothermal reaction. Then a sol–gel process was utilized to prepare silica coated Fe_3O_4 microspheres (Fe_3O_4@SiO_2), and a thin amorphous silica layer was formed on Fe_3O_4 microspheres. Afterward, the Fe_3O_4@SiO_2 microspheres were modified by 3-(methacryloxypropyl) trimethoxysilane (MPS). Finally, the triblock copolymer was fabricated by aqueous phase radical copolymerization reaction among MPS, divinylbenzene (DVB) and N-Vinyl-2-pyrrolidone (NVP) on the surface of Fe_3O_4@SiO_2. The magnetic Fe_3O_4 particles with narrow size distribution have nearly spherical shape and smooth surface. Li et al. [124] reported hexagonal and triangular monodisperse Fe_3O_4 nanosheets by a two-step microemulsion

Lv *et al. Nanoscale Res Lett*   (2021) 16:138

Page 13 of 19

solvothermal approach, in which the uniform Fe_3O_4 nanoparticles are prepared and then these hydrophobic nanocrystals are dispersed in a uniform microemulsion environment as "seeds" for further re-growth through a secondary solvothermal process. In the first step, near-spherical monodisperse 7–8 nm Fe_3O_4 nanoparticles were formed through a kinetically controlled process. In the second step, the formation of anisotropic Fe_3O_4 nanosheets is a thermodynamically controlled process and all the exposed surfaces of the triangular and hexagonal nanosheets are (111) crystal planes, which have the lowest surface energy for FCC Fe_3O_4.

Other Methods

Physical methods are also significant ways to prepared Fe_3O_4 nanostructure for anode of LIBs. Several advantages, such as good crystallization, fine-tuned particle size, and high purity of products are highlighted in recent literatures. But these methods usually demand advanced and expensive equipment, result in a higher cost, poor dispensability of particles dispersion, and agglomeration of nanostructures. For instance, Du et al. [109] fabricated activated carbon (AC)-Fe_3O_4 nanoparticles asymmetric supercapacitor, and Fe_3O_4 nanostructure was prepared by microwave method. The precursor, $FeSO_4 \cdot 7H_2O$ and $NH_3 \cdot H_2O$ mixed solution, was heated in microwave oven. The black precipitate was separated by magnet and washed repeatedly with DI water. The resulted microstructural properties of prepared nanoparticle were characterized by nitrogen adsorption (Quantachrome NOVA 2000), XRD and SEM [109]. Chen et al. [127] synthesized graphene nanosheets decorated with ultra-small Fe_3O_4 nanoparticles (USIO/G). Seo et al. [134] reported an integrated usage of magnetic particles in microalgal downstream processes, specifically microalgal harvesting and lipid extraction through one-step aerosol spray pyrolysis and applied in microalgal harvesting and serial microalgal lipid entrapment. TEM/EDS, XPS, and FT-IR analysis suggested that the cationic and lipophilic functionalities arose from not fully decomposed PVP, due to the short residence time in the reactor. Kang et al. [135] proposed Fe_3O_4 nanocrystals confined in mesocellular carbon foam

(MSU-F–C) by a "host–guest" approach and applied it as LIBs anode. In this study, a precursor of $Fe(NO_3)_3 \cdot 9H_2O$ is impregnated in MSU-F–C having uniform cellular pores with a diamter of ~30 nm, followed by heating treatment at 400 °C for 4 h in argon (Ar) atmosphere. Fe_3O_4 nanocrystals with size of 13–27 nm were fabricated inside the pores of MSU-F–C. The existance of the carbon most likely allows the reduction of some Fe^{3+} to Fe^{2+} ions by a carbothermoreduction process. The physical performance and pore structure of MSU-F–C and Fe_3O_4-loaded composites were characterized with nitrogen sorption, and the composites have high capacities of ~800–1000 mA h g^{-1} at 0.1 A g^{-1} (~0.1 C rate), high rate capability and good cycling performance.

Application

Fe_3O_4 possesses lots of unique properties, and is highly promising for applications in LIBs and supercapacitors [136–142]. Table 4 summarizes some applications.
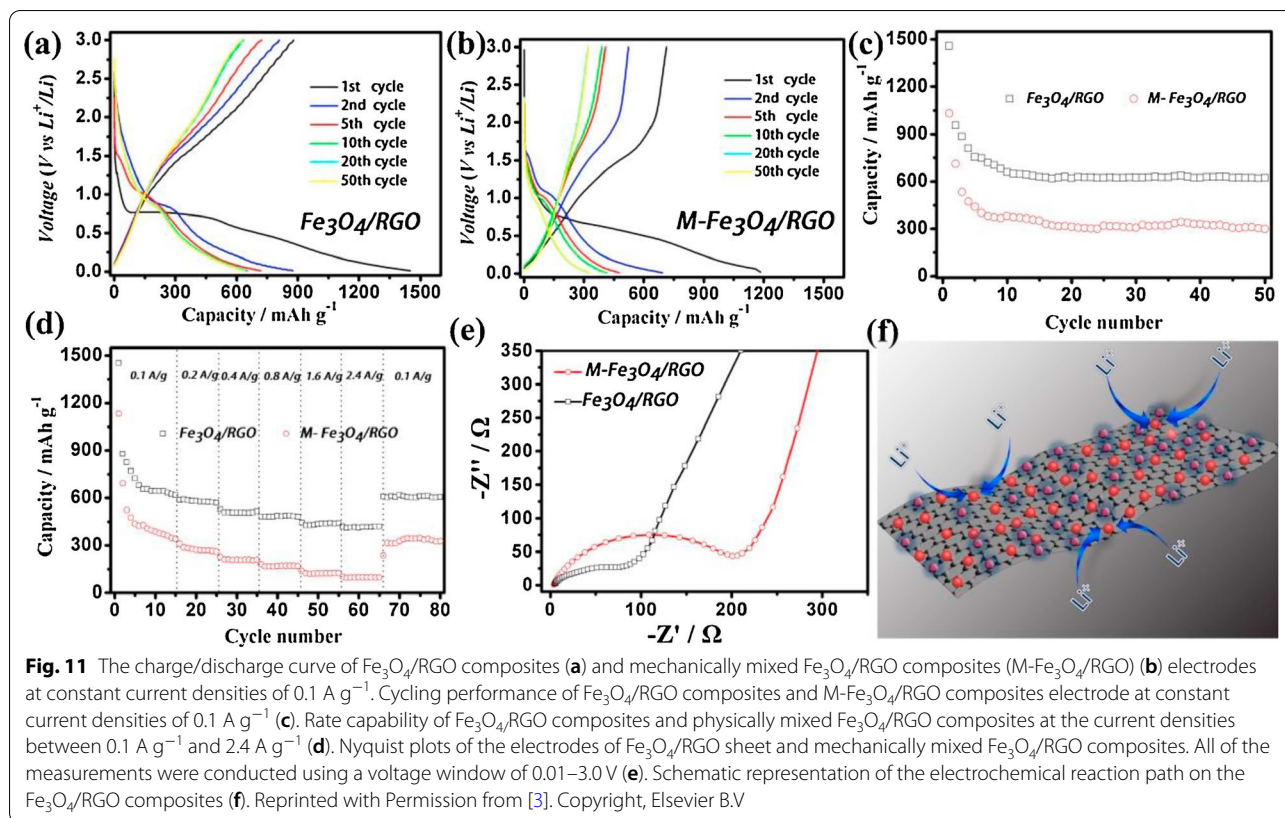
Li-Ion Batteries

Due to conversion reaction of Fe_3O_4 during charge/discharge process and other advantages, the Fe_3O_4 is usually studied and applied as LIBs anode [143–147]. For TMOs, they have higher theoretical capacity (~500–1000 mA h g^{-1}) than conventional graphite (about 372 mA h g^{-1}). Furthermore, Fe_3O_4 has superior conductivity compared with other transition metal oxides. Thus, it is well-focused by recent studies. It has been reported that composite electrodes with graphene have high performance due to their large surface area, high electrical conductivity and adaptive or flexible structure for high reliability. Qiu et al. [3] reported a kind of composite anode composed of ultra-dispersed Fe_3O_4 nanoparticles (3–8 nm) and RGO sheet. It has excellent cyclic performance (624 mA h g^{-1} for up to 50 charge/discharge cycles at a current density of 0.1 A g^{-1}), and good specific capability (624 and 415 mAh g^{-1} at 0.1 and 2.4 A g^{-1}, respectively) for LIBs. The obtained Fe_3O_4/RGO exhibited high and ultrastable Photo-Fenton activity (Fig. 11).

Pyrolyzed carbon is also a good "companion" for Fe_3O_4 anodes. Apart from the facile protocol, porous

Table 4 A Summary of synthesis and electrochemical performance of Fe_3O_4 based nanostructures

Structure	Synthesis	Electrochemical performance	Ref
Fe_3O_4 nanoparticles	Hydrothermal synthesis	Capacitance of 207.7 F g^{-1} at 0.4 A g^{-1}; retention of 100% after 2000 cycles	[106]
Hierarchical porous Fe_3O_4/graphene nanowires	Hydrothermal synthesis	Capacity of 1146 mA h g^{-1} at 5 A g^{-1}	[51]
Fe_3O_4 particles/carbon nanonetworks	Thermolysis	Capacity of 1534 mA h g^{-1} at a 1 C; without decay up to 500 cycles (1 C = 1 A g^{-1})	[109]
Fe_3O_4 doped double-shelled hollow carbon spheres	Rapid aerosol	Capacitance of 1153 F g^{-1} at 2 A g^{-1}; retention of 96.7% after 8000 cycles	[4]

Fig. 11 The charge/discharge curve of Fe_3O_4/RGO composites (**a**) and mechanically mixed Fe_3O_4/RGO composites (M-Fe_3O_4/RGO) (**b**) electrodes at constant current densities of 0.1 A g^{-1}. Cycling performance of Fe_3O_4/RGO composites and M-Fe_3O_4/RGO composites electrode at constant current densities of 0.1 A g^{-1} (**c**). Rate capability of Fe_3O_4/RGO composites and physically mixed Fe_3O_4/RGO composites at the current densities between 0.1 A g^{-1} and 2.4 A g^{-1} (**d**). Nyquist plots of the electrodes of Fe_3O_4/RGO sheet and mechanically mixed Fe_3O_4/RGO composites. All of the measurements were conducted using a voltage window of 0.01–3.0 V (**e**). Schematic representation of the electrochemical reaction path on the Fe_3O_4/RGO composites (**f**). Reprinted with Permission from [3]. Copyright, Elsevier B.V

structure formed by pyrolysis always exhibits high specific capacity of Fe_3O_4 composite anode. Wang et al. [12] reported hollow N-doped Fe_3O_4/C nanocages with hierarchical porosities by carbonizing polydopamine-coated PB nanocrystals as LIBs anode (Fig. 12). The specific capacity of N-doped Fe_3O_4/C nanocages is ~ 878.7 mA h g^{-1} after 200 cycles at a current density of 200 mA g^{-1}, much higher than that of N-doped Fe_3O_4/C derived from pure PB (merely 547 mA h g^{-1}). It is also desirable to design anisotropic structure of Fe_3O_4 nanoparticles with carbon coated layer. Zhang et al. [19] reported a kind of carbon-coated Fe_3O_4 nanospindles derived from α-Fe_2O_3 nanospindles with length of about 500 nm and an axis ratio of ~ 4. Following by a hydrothermal synthesis method with glucose, the obtained LIBs anode delivered a high reversible capacity of ~ 745 mA h g^{-1} at C/5 and ~ 600 mA h g^{-1} at C/2.

The most impressive work towards this field is probably the mesoporous iron oxide nanoparticle clusters with carbon coating reported by Lee et al. [148]. After a few cycles, the formation of SEI greatly enhanced the stability of interface between electrode and electrolyte. Electrochemical test exhibited a high specific capacity of 970 mA h g^{-1} for LIBs.

Supercapacitors

Fe_3O_4 is a highly promising candidate for supercapacitor electrode because of its relatively high electrical conductivity, fast reversible redox reaction, low cost and eco-friendly nature [149–152]. Similar to batteries, high performance supercapacitors also require two factors: large specific surface area and long-term stability. Those two features usually were achieved by building some porous structures and carbon coated layers. Fe_3O_4 nanoparticle with a high specific surface area was synthesized by Wang et al. [126] using a bottom up approach. Ferric chloride was firstly sonicated with ethanolamine and then processed through a solvothermal reaction. The obtained active nanomaterials showed a specific surface area of 165.05 m^2 g^{-1} and a specific capacitance of 207.7 F g^{-1} at 0.4 A g^{-1}.

Also, highly dispersed Fe_3O_4 nanosheets on 1D CNFs is reported by Mu et al. [125]. The Fe_3O_4/CNFs composites showed a higher specific capacitance than pure Fe_3O_4 in 1 M Na_2SO_4. To further enlarge the specific capacitance and cycle stability, hierarchically porous carbon spheres with Fe_3O_4 using as supercapacitors exhibited high capacitivity of 1153 F g^{-1} at 2 A g^{-1} and high specific capacitance of 514 F g^{-1} at 100 A g^{-1}. In addition, the assembled asymmetric supercapacitor with

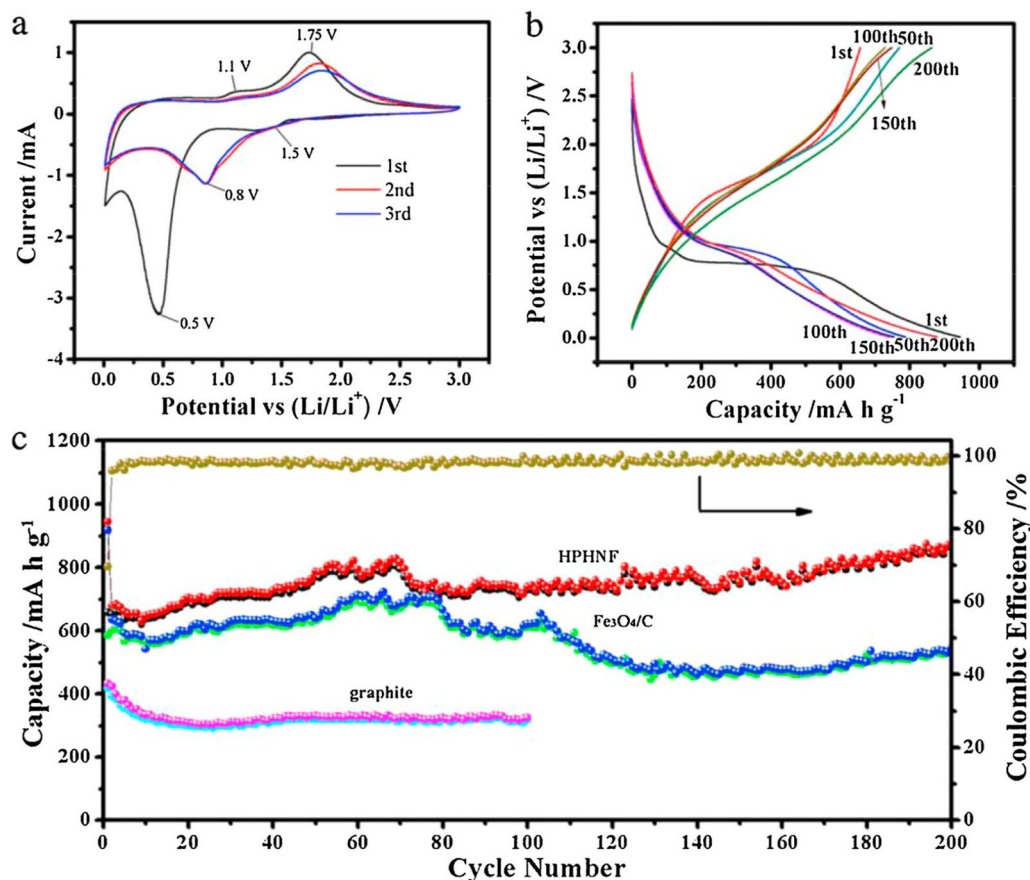Lv *et al. Nanoscale Res Lett*   (2021) 16:138

Page 15 of 19

Fig. 12 a CVs of the HPHNF during the first three cycles at 0.2 mV s^{-1}, **b** Galvanostatic charge/discharge profiles of the HPHNF electrodes for the 1st, 50th, 100th, 150th and 200th cycle at a specific current of 200 mA g^{-1}. **c** Cycling performance of the HPHNF nanocomposites, N-doped Fe$_3$O$_4$/C nanocomposites and graphite at a specific current of 200 mA g^{-1}. **d** Coulombic efficiency of HPHNF. Reprinted with Permission from [12], Copyright, Elsevier Ltd

double-shelled hollow carbon spheres and Fe$_3$O$_4$, has excellent cycling stability (96.7% retention after 8000 cycles) and high energy density (17–45 Wh kg^{-1}) at a power density of 400–8000 W kg^{-1} [4].

Conclusion

Iron oxides (Fe$_{1-x}$O, Fe$_2$O$_3$, Fe$_3$O$_4$) based nanostructures have much higher specific capacities than those of commercial carbon based anodes. They are considered as highly promising candidates for LIBs anode. However, large irreversible capacity and low cycle stability are two serious problems that obstruct the application of iron oxides based nanostructures. In this review, we summarized the recent progress on novel iron oxides and their composites as LIBs anode and supercapacitor electrode. Several typical synthetic methods of various novel iron oxides based nanostructures are listed. By comparing the electrochemical performance of these various iron oxides based nanostructures, some strategies are expected to solve the problems of iron oxides based nanostructures.

Declarations

Competing interests
The authors declare that they have no competing interests.

Author details
[1]School of Mechanical Engineering, Sichuan University, Chengdu 610065, People's Republic of China. [2]State Key Laboratory of Advanced Technology for Materials Synthesis and Processing, Wuhan University of Technology, Wuhan 430070, People's Republic of China. [3]Med+X Center

Lv *et al. Nanoscale Res Lett*   (2021) 16:138

Page 16 of 19

for Manufacturing, West China Hospital, Sichuan University, Chengdu 610041, People's Republic of China.

References

1. Li H, Zhu Y-J (2020) Liquid-phase synthesis of iron oxide nanostructured materials and their applications. Chem Eur J 26:9180–9205. https://doi.org/10.1002/chem.202000679
2. Pu J, Shen Z, Zhong C et al (2019) Electrodeposition technologies for Li-based batteries: new frontiers of energy storage. Adv Mater 32:1903808. https://doi.org/10.1002/adma.201903808
3. Qiu B, Li Q, Shen B et al (2016) Stöber-like method to synthesize ultradispersed Fe_3O_4 nanoparticles on graphene with excellent Photo-Fenton reaction and high-performance lithium storage. Appl Catal B 183:216–223. https://doi.org/10.1016/j.apcatb.2015.10.053
4. Li X, Zhang L, He G (2016) Fe_3O_4 doped double-shelled hollow carbon spheres with hierarchical pore network for durable high-performance supercapacitor. Carbon 99:514–522. https://doi.org/10.1016/j.carbon.2015.12.076
5. Khan I, Khalil A, Khanday F et al (2018) Synthesis, Characterization and Applications of Magnetic Iron Oxide Nanostructures. Arab J Sci Eng 43:43–61. https://doi.org/10.1007/s13369-017-2835-1
6. Zhu L, Chang Z, Wang Y et al (2015) Core–shell $MnO_2@Fe_2O_3$ nanospindles as a positive electrode for aqueous supercapacitors. J Mater Chem A 3:22066–22072. https://doi.org/10.1039/C5TA05556C
7. Zhang L, Zhao K, Xu W et al (2015) Integrated SnO_2 nanorod array with polypyrrole coverage for high-rate and long-life lithium batteries. Phys Chem Chem Phys 17:7619–7623. https://doi.org/10.1039/C5CP00150A
8. Zhang C, Liu W, Chen D et al (2015) One step hydrothermal synthesis of $FeCO_3$ cubes for high performance lithium-ion battery anodes. Electrochim Acta 182:559–564. https://doi.org/10.1016/j.electacta.2015.09.137
9. Xia H, Hong C, Li B et al (2015) Facile synthesis of hematite quantum-dot/functionalized graphene-sheet composites as advanced anode materials for asymmetric supercapacitors. Adv Funct Mater 25:627–635. https://doi.org/10.1002/adfm.201403554
10. Wei Q, Liu J, Feng W et al (2015) Hydrated vanadium pentoxide with superior sodium storage capacity. J Mater Chem A 3:8070–8075. https://doi.org/10.1039/C5TA00502G
11. Jung D-W, Jeong J-H, Han S-W, Oh E-S (2016) Electrochemical performance of potassium-doped wüstite nanoparticles supported on graphene as an anode material for lithium ion batteries. J Power Sources 315:16–22. https://doi.org/10.1016/j.jpowsour.2016.03.022
12. Wang L, Wu J, Chen Y et al (2015) Hollow nitrogen-doped Fe_3O_4/carbon nanocages with hierarchical porosities as anode materials for lithium-ion batteries. Electrochim Acta 186:50–57. https://doi.org/10.1016/j.electacta.2015.10.134
13. Xu Y, Jian G, Liu Y et al (2014) Superior electrochemical performance and structure evolution of mesoporous Fe_2O_3 anodes for lithium-ion batteries. Nano Energy 3:26–35. https://doi.org/10.1016/j.nanoen.2013.10.003
14. Wang H, Zhou Y, Shen Y et al (2015) Fabrication, formation mechanism and the application in lithium-ion battery of porous Fe_2O_3 nanotubes via single-spinneret electrospinning. Electrochim Acta 158:105–112. https://doi.org/10.1016/j.electacta.2015.01.149
15. Wan Y, Yang Z, Xiong G et al (2015) Anchoring Fe_3O_4 nanoparticles on three-dimensional carbon nanofibers toward flexible high-performance anodes for lithium-ion batteries. J Power Sources 294:414–419. https://doi.org/10.1016/j.jpowsour.2015.06.057
16. Zhang L, Wu HB, Lou XWD (2014) Iron-oxide-based advanced anode materials for lithium-ion batteries. Adv Energy Mater 4:1300958. https://doi.org/10.1002/aenm.201300958
17. Wang M-S, Fan L-Z (2013) Silicon/carbon nanocomposite pyrolyzed from phenolic resin as anode materials for lithium-ion batteries. J Power Sources 244:570–574. https://doi.org/10.1016/j.jpowsour.2013.01.151
18. Pan Q, Huang K, Ni S et al (2009) Synthesis of α-Fe_2O_3 dendrites by a hydrothermal approach and their application in lithium-ion batteries. J Phys D: Appl Phys 42:015417. https://doi.org/10.1088/0022-3727/42/1/015417
19. Zhang W-M, Wu X-L, Hu J-S et al (2008) Carbon coated Fe_3O_4 nanospindles as a superior anode material for lithium-ion batteries. Adv Funct Mater 18:3941–3946. https://doi.org/10.1002/adfm.200801386
20. Reddy MV, Yu T, Sow CH et al (2007) α-Fe_2O_3 nanoflakes as an anode material for Li-ion batteries. Adv Funct Mater 17:2792–2799. https://doi.org/10.1002/adfm.200601186
21. Ng SH, Wang J, Konstantinov K et al (2007) Spray-pyrolyzed silicon/disordered carbon nanocomposites for lithium-ion battery anodes. J Power Sources 174:823–827. https://doi.org/10.1016/j.jpowsour.2007.06.165
22. Zhao L, Watanabe I, Doi T et al (2006) TG-MS analysis of solid electrolyte interphase (SEI) on graphite negative-electrode in lithium-ion batteries. J Power Sources 161:1275–1280. https://doi.org/10.1016/j.jpowsour.2006.05.045
23. Ye W, Pei F, Lan X et al (2020) Stable nano-encapsulation of lithium through seed-free selective deposition for high-performance Li battery anodes. Adv Energy Mater 10:1902956. https://doi.org/10.1002/aenm.201902956
24. Francis CFJ, Kyratzis IL, Best AS (2020) Lithium-ion battery separators for ionic-liquid electrolytes: a review. Adv Mater 32:1904205. https://doi.org/10.1002/adma.201904205
25. Zhang H, Zhou L, Noonan O et al (2014) Tailoring the void size of iron oxide@carbon yolk-shell structure for optimized lithium storage. Adv Funct Mater 24:4337–4342. https://doi.org/10.1002/adfm.201400178
26. Chan CK, Peng H, Liu G et al (2008) High-performance lithium battery anodes using silicon nanowires. Nature Nanotech 3:31–35. https://doi.org/10.1038/nnano.2007.411
27. Zhang G, Hou S, Zhang H et al (2015) High-performance and ultra-stable lithium-ion batteries based on MOF-derived ZnO@ZnO quantum dots/C core-shell nanorod arrays on a carbon cloth anode. Adv Mater 27:2400–2405. https://doi.org/10.1002/adma.201405222
28. Mehta V, Saini HS, Srivastava S et al (2021) Assessment of Mo_2N monolayer as Li-ion battery anodes with high cycling stability. Mater Today Commun 26:102100. https://doi.org/10.1016/j.mtcomm.2021.102100
29. Wu J, Guo G, Zhu J et al (2021) Synthesis and research of $(Ni_{0.1}Co_{0.3}Mn_{0.6})_3O_4$ as lithium-ion battery conversion-type anode using spent $LiNi_{0.6}Co_{0.2}Mn_{0.2}O_2$ batteries. Int J Energy Res 45:13298–13306. https://doi.org/10.1002/er.6655
30. Poizot P, Laruelle S, Grugeon S et al (2000) Nano-sized transition-metal oxides as negative-electrode materials for lithium-ion batteries. Nature 407:496–499. https://doi.org/10.1038/35035045
31. Gao M, Zhou P, Wang P et al (2013) FeO/C anode materials of high capacity and cycle stability for lithium-ion batteries synthesized by carbothermal reduction. J Alloys Compd 565:97–103. https://doi.org/10.1016/j.jallcom.2013.03.012
32. Zhao Y, Li X, Yan B et al (2016) Recent developments and understanding of novel mixed transition-metal oxides as anodes in lithium ion batteries. Adv Energy Mater 6:1502175. https://doi.org/10.1002/aenm.201502175
33. Zhi J, Li S, Han M et al (2018) Unveiling conversion reaction on intercalation-based transition metal oxides for high power, high energy aqueous lithium battery. Adv Energy Mater 8:1802254. https://doi.org/10.1002/aenm.201802254
34. Li S, Dong Y, Xu L et al (2014) Effect of carbon matrix dimensions on the electrochemical properties of $Na_3V_2(PO_4)_3$ nanograins for high-performance symmetric sodium-ion batteries. Adv Mater 26:3545–3553. https://doi.org/10.1002/adma.201305522
35. Shin J, Lee KY, Yeo T, Choi W (2016) Facile one-pot transformation of iron oxides from Fe_2O_3 nanoparticles to nanostructured $Fe_3O_4@C$ core-shell composites via combustion waves. Sci Rep 6:21792. https://doi.org/10.1038/srep21792
36. Li H, Su Y, Sun W, Wang Y (2016) Carbon nanotubes rooted in porous ternary metal sulfide@N/S-doped carbon dodecahedron: bimetal-organic-frameworks derivation and electrochemical application for high-capacity and long-life lithium-ion batteries. Adv Funct Mater 26:8345–8353. https://doi.org/10.1002/adfm.201601631
37. Mo R, Rooney D, Sun K, Yang HY (2017) 3D nitrogen-doped graphene foam with encapsulated germanium/nitrogen-doped graphene

Lv *et al. Nanoscale Res Lett*   (2021) 16:138

Page 17 of 19

yolk-shell nanoarchitecture for high-performance flexible Li-ion battery. Nat Commun 8:13949. https://doi.org/10.1038/ncomms13949

38. Cui Z, He S, Liu Q et al (2020) Graphene-like carbon film wrapped Tin(II) sulfide nanosheet arrays on porous carbon fibers with enhanced electrochemical kinetics as high-performance Li and Na ion battery anodes. Adv Sci 7:1903045. https://doi.org/10.1002/advs.201903045

39. Hrynkiewicz HU, Kulgawczuk DS, Mazanek ES et al (1972) Mössbauer effect studies of ferrous oxides $Fe_{1-x}O$. Phys Stat Sol (a) 9:611–616. https://doi.org/10.1002/pssa.2210090225

40. Gohy C, Gérard A, Grandjean F (1982) Mössbauer Study of Wustite and Mangano-Wustite. Phys Status Solidi A 74:583–591. https://doi.org/10.1002/pssa.2210740225

41. Tiwari A (1998) Local environment of Fe in $NdFe_{1-x}Ni_xO_{3-\delta}$ perovskite oxides. J Alloys Compd 274:42–46. https://doi.org/10.1016/S0925-8388(98)00553-2

42. Aldon L, Jumas J-C (2012) Lithium-induced conversion reaction in wüstite $Fe_{1-x}O$ studied by ^{57}Fe Mössbauer spectroscopy. Solid State Sci 14:354–361. https://doi.org/10.1016/j.solidstatesciences.2011.12.006

43. Roth WL (1969) Experimental magnetochemistry. Nonmetallic magnetic materials by M. M Schieber. Acta Crystallogr B Struct Sci 25:1217–1218. https://doi.org/10.1107/S0567740869003827

44. Xu X, Cao R, Jeong S, Cho J (2012) Spindle-like mesoporous $\alpha-Fe_2O_3$ anode material prepared from MOF template for high-rate lithium batteries. Nano Lett 12:4988–4991. https://doi.org/10.1021/nl302618s

45. Wang X, Xiao Y, Hu C, Cao M (2014) A dual strategy for improving lithium storage performance, a case of Fe_2O_3. Mater Res Bull 59:162–169. https://doi.org/10.1016/j.materresbull.2014.07.008

46. Cao K, Jiao L, Liu H et al (2015) 3D Hierarchical Porous $\alpha-Fe_2O_3$ nanosheets for high-performance lithium-ion batteries. Adv Energy Mater 5:1401421. https://doi.org/10.1002/aenm.201401421

47. Zhu X, Zhu Y, Murali S et al (2011) Nanostructured reduced graphene oxide/Fe_2O_3 composite as a high-performance anode material for lithium ion batteries. ACS Nano 5:3333–3338. https://doi.org/10.1021/nn200493r

48. Lin Y-M, Abel PR, Heller A, Mullins CB (2011) $\alpha-Fe_2O_3$ nanorods as anode material for lithium ion batteries. J Phys Chem Lett 2:2885–2891. https://doi.org/10.1021/jz201363j

49. Jiang T, Bu F, Feng X et al (2017) Porous Fe_2O_3 nanoframeworks encapsulated within three-dimensional graphene as high-performance flexible anode for lithium-ion battery. ACS Nano 11:5140–5147. https://doi.org/10.1021/acsnano.7b02198

50. Yin L, Gao YJ, Jeon I et al (2019) Rice-panicle-like $\gamma-Fe_2O_3@C$ nanofibers as high-rate anodes for superior lithium-ion batteries. Chem Eng J 356:60–68. https://doi.org/10.1016/j.cej.2018.09.017

51. Lin Y, Zhou S, Sheehan SW, Wang D (2011) Nanonet-based hematite heteronanostructures for efficient solar water splitting. J Am Chem Soc 133:2398–2401. https://doi.org/10.1021/ja110741z

52. Vayssieres L, Beermann N, Lindquist S-E, Hagfeldt A (2001) Controlled aqueous chemical growth of oriented three-dimensional crystalline nanorod arrays: application to Iron(III) oxides. Chem Mater 13:233–235. https://doi.org/10.1021/cm001202x

53. Kleiman-Shwarscstein A, Huda MN, Walsh A et al (2010) Electrodeposited aluminum-doped $\alpha-Fe_2O_3$ photoelectrodes: experiment and theory. Chem Mater 22:510–517. https://doi.org/10.1021/cm903135j

54. Zhang L, Wu HB, Madhavi S et al (2012) Formation of Fe_2O_3 microboxes with hierarchical shell structures from metal-organic frameworks and their lithium storage properties. J Am Chem Soc 134:17388–17391. https://doi.org/10.1021/ja307475c

55. Ramos Guivar JA, Sanches EA, Bruns F et al (2016) Vacancy ordered $\gamma-Fe_2O_3$ nanoparticles functionalized with nanohydroxyapatite: XRD, FTIR, TEM, XPS and Mössbauer studies. Appl Surf Sci 389:721–734. https://doi.org/10.1016/j.apsusc.2016.07.157

56. Bashir AKH, Furqan CM, Bharuth-Ram K et al (2019) Structural, optical and Mössbauer investigation on the biosynthesized $\alpha-Fe_2O_3$: Study on different precursors. Phys E Low Dimens Syst 111:152–157. https://doi.org/10.1016/j.physe.2019.03.010

57. He L, Liu H, Luo W et al (2019) One-step electrodeposited $Mn_xCo_{1-x}(OH)_2$ nanosheet arrays as cathode for asymmetric on-chip micro-supercapacitors. Appl Phys Lett 114:223903. https://doi.org/10.1063/1.5090290

58. He L, Hong T, Hong X et al (2019) Ultrastable high-energy on-chip nickel-bismuth microbattery powered by crystalline Bi anode and Ni–Co hydroxide cathode. Energy Technol 7:1900144. https://doi.org/10.1002/ente.201900144

59. Ma X, Feng S, He L et al (2017) Rapid, all dry microfabrication of three-dimensional Co_3O_4/Pt nanonetworks for high-performance micro-supercapacitors. Nanoscale 9:11765–11772. https://doi.org/10.1039/C7NR01789H

60. An Z, He L, Toda M et al (2015) Microstructuring of carbon nanotubes-nickel nanocomposite. Nanotechnology 26:195601. https://doi.org/10.1088/0957-4484/26/19/195601

61. Yang Y, Fan X, Casillas G et al (2014) Three-dimensional nanoporous Fe_2O_3/Fe_3C-graphene heterogeneous thin films for lithium-ion batteries. ACS Nano 8:3939–3946. https://doi.org/10.1021/nn500865d

62. Kay A, Cesar I, Grätzel M (2006) New benchmark for water photooxidation by nanostructured $\alpha-Fe_2O_3$ films. J Am Chem Soc 128:15714–15721. https://doi.org/10.1021/ja064380l

63. Wu J-J, Lee Y-L, Chiang H-H, Wong DK-P (2006) Growth and magnetic properties of oriented $\alpha-Fe_2O_3$ nanorods. J Phys Chem B 110:18108–18111. https://doi.org/10.1021/jp0644661

64. Jia L, Harbauer K, Bogdanoff P et al (2015) Sputtering deposition of ultra-thin $\alpha-Fe_2O_3$ films for solar water splitting. J Mater Sci Technol 31:655–659. https://doi.org/10.1016/j.jmst.2014.10.007

65. Zhong L-S, Hu J-S, Liang H-P et al (2006) Self-assembled 3D flowerlike iron oxide nanostructures and their application in water treatment. Adv Mater 18:2426–2431. https://doi.org/10.1002/adma.200600504

66. Wu Z, Yu K, Zhang S, Xie Y (2008) Hematite hollow spheres with a mesoporous shell: controlled synthesis and applications in gas sensor and lithium ion batteries. J Phys Chem C 112:11307–11313. https://doi.org/10.1021/jp803582d

67. Yang Y, Ma H, Zhuang J, Wang X (2011) Morphology-controlled synthesis of hematite nanocrystals and their facet effects on gas-sensing properties. Inorg Chem 50:10143–10151. https://doi.org/10.1021/ic201104w

68. Woo K, Lee HJ, Ahn J-P, Park YS (2003) Sol–gel mediated synthesis of Fe_2O_3 nanorods. Adv Mater 15:1761–1764. https://doi.org/10.1002/adma.200305561

69. Hu X, Yu JC, Gong J et al (2007) $\alpha-Fe_2O_3$ nanorings prepared by a microwave-assisted hydrothermal process and their sensing properties. Adv Mater 19:2324–2329. https://doi.org/10.1002/adma.200602176

70. Wen X, Wang S, Ding Y et al (2005) Controlled growth of large-area, uniform, vertically aligned arrays of $\alpha-Fe_2O_3$ nanobelts and nanowires. J Phys Chem B 109:215–220. https://doi.org/10.1021/jp0461448

71. Rao PM, Zheng X (2009) Rapid catalyst-free flame synthesis of dense, aligned $\alpha-Fe_2O_3$ nanoflake and CuO nanoneedle arrays. Nano Lett 9:3001–3006. https://doi.org/10.1021/nl901426t

72. Cvelbar U, Chen Z, Sunkara MK, Mozetič M (2008) Spontaneous growth of superstructure $a-Fe_2O_3$ nanowire and nanobelt arrays in reactive oxygen plasma. Small 4:1610–1614. https://doi.org/10.1002/smll.200800278

73. Kim JH, Hong YJ, Kang YC et al (2015) Superior electrochemical properties of $\alpha-Fe_2O_3$ nanofibers with a porous core/dense shell structure formed from iron acetylacetonate-polyvinylpyrrolidone composite fibers. Electrochim Acta 154:211–218. https://doi.org/10.1016/j.electacta.2014.11.181

74. Zhou W, Cheng C, Liu J et al (2011) Epitaxial growth of branched $\alpha-Fe_2O_3$/SnO_2 nano-heterostructures with improved lithium-ion battery performance. Adv Funct Mater 21:2439–2445. https://doi.org/10.1002/adfm.201100088

75. LaTempa TJ, Feng X, Paulose M, Grimes CA (2009) Temperature-dependent growth of self-assembled hematite ($\alpha-Fe_2O_3$) nanotube arrays: rapid electrochemical synthesis and photoelectrochemical properties. J Phys Chem C 113:16293–16298. https://doi.org/10.1021/jp904560n

76. Prakasam HE, Varghese OK, Paulose M et al (2006) Synthesis and photoelectrochemical properties of nanoporous iron(III) oxide by potentiostatic anodization. Nanotechnology 17:4285–4291. https://doi.org/10.1088/0957-4484/17/17/001

77. Mao A, Han GY, Park JH (2010) Synthesis and photoelectrochemical cell properties of vertically grown $\alpha-Fe_2O_3$ nanorod arrays on a gold nanorod substrate. J Mater Chem 20:2247. https://doi.org/10.1039/b921965j

Lv *et al. Nanoscale Res Lett* (2021) 16:138

Page 18 of 19

78. Duret A, Grätzel M (2005) Visible light-induced water oxidation on mesoscopic α-Fe$_2$O$_3$ films made by ultrasonic spray pyrolysis. J Phys Chem B 109:17184–17191. https://doi.org/10.1021/jp044127c

79. Liu X, Fan H, Li B et al (2019) α-Fe$_2$O$_3$ hollow microspheres assembled by ultra-thin nanoflakes exposed with (241) high-index facet: Solvothermal synthesis, lithium storage performance, and superparamagnetic property. Int J Hydrogen Energy 44:1070–1077. https://doi.org/10.1016/j.ijhydene.2018.11.043

80. Ristić M, Reissner M, Krehula S, Musić S (2018) ^{57}Fe Mössbauer spectroscopic study and magnetic properties of 1D Fe(IO$_3$)$_3$ particles and their thermal decomposition to α-Fe$_2$O$_3$. Mater Lett 227:47–50. https://doi.org/10.1016/j.matlet.2018.05.049

81. Mund HS, Ahuja BL (2017) Structural and magnetic properties of Mg doped cobalt ferrite nano particles prepared by sol-gel method. Mater Res Bull 85:228–233. https://doi.org/10.1016/j.materresbull.2016.09.027

82. Lyubutin IS, Gervits NE, Starchikov SS et al (2015) Magnetic and Mössbauer spectroscopy studies of hollow microcapsules made of silica-coated CoFe$_2$O$_4$ nanoparticles. Smart Mater Struct 25:015022. https://doi.org/10.1088/0964-1726/25/1/015022

83. Larcher D, Bonnin D, Cortes R et al (2003) Combined XRD, EXAFS, and Mössbauer studies of the reduction by lithium of α-Fe$_2$O$_3$ with various particle sizes. J Electrochem Soc 150:A1643. https://doi.org/10.1149/1.1622959

84. Morales J, Sánchez L, Martín F et al (2004) Nanostructured CuO thin film electrodes prepared by spray pyrolysis: a simple method for enhancing the electrochemical performance of CuO in lithium cells. Electrochim Acta 49:4589–4597. https://doi.org/10.1016/j.electacta.2004.05.012

85. Wang B, Chen JS, Wu HB et al (2011) Quasiemulsion-templated formation of α-Fe$_2$O$_3$ hollow spheres with enhanced lithium storage properties. J Am Chem Soc 133:17146–17148. https://doi.org/10.1021/ja208346s

86. Park J, Yoo H, Choi J (2019) 3D ant-nest network of α-Fe$_2$O$_3$ on stainless steel for all-in-one anode for Li-ion battery. J Power Sources 431:25–30. https://doi.org/10.1016/j.jpowsour.2019.05.054

87. Liu H, Luo S, Zhang D et al (2019) A simple and low-cost method to synthesize Cr-Doped α-Fe$_2$O$_3$ electrode materials for lithium-ion batteries. ChemElectroChem 6:856–864. https://doi.org/10.1002/celc.201801736

88. Park C, Samuel E, Joshi B et al (2020) Supersonically sprayed Fe$_2$O$_3$/C/CNT composites for highly stable Li-ion battery anodes. Chem Eng J 395:125018. https://doi.org/10.1016/j.cej.2020.125018

89. Wang Q, Wang Q, Zhang D-A et al (2014) Core-shell α-Fe$_2$O$_3$@α-MoO$_3$ nanorods as lithium-ion battery anodes with extremely high capacity and cyclability. Chem Asian J 9:3299–3306. https://doi.org/10.1002/asia.201402809

90. Jeong J-M, Choi BG, Lee SC et al (2013) Hierarchical hollow spheres of Fe$_2$O$_3$@polyaniline for lithium ion battery anodes. Adv Mater 25:6250–6255. https://doi.org/10.1002/adma.201302710

91. Teng X, Qin Y, Wang X et al (2018) A nanocrystalline Fe$_2$O$_3$ film anode prepared by pulsed laser deposition for lithium-ion batteries. Nanoscale Res Lett 13:60. https://doi.org/10.1186/s11671-018-2475-8

92. Khatoon R, Guo Y, Attique S et al (2020) Facile synthesis of α-Fe$_2$O$_3$/Nb$_2$O$_5$ heterostructure for advanced Li-Ion batteries. J Alloys Compd 837:155294. https://doi.org/10.1016/j.jallcom.2020.155294

93. Wang R, Xu C, Sun J, Gao L (2015) Three-dimensional Fe$_2$O$_3$ nanocubes/nitrogen-doped graphene aerogels: nucleation mechanism and lithium storage properties. Sci Rep 4:7171. https://doi.org/10.1038/srep07171

94. Qu D, Sun Z, Gan S et al (2020) Two-dimensional Fe$_2$O$_3$/TiO$_2$ composite nanoplates with improved lithium storage properties as anodic materials for lithium-ion full cells. ChemElectroChem 7:4963–4970. https://doi.org/10.1002/celc.202001143

95. Chen J, Xu L, Li W, Gou X (2005) α-Fe$_2$O$_3$ nanotubes in gas sensor and lithium-ion battery applications. Adv Mater 17:582–586. https://doi.org/10.1002/adma.200401101

96. Lu X, Yu M, Wang G et al (2014) Flexible solid-state supercapacitors: design, fabrication and applications. Energy Environ Sci 7:2160. https://doi.org/10.1039/c4ee00960f

97. Lu X, Zeng Y, Yu M et al (2014) Oxygen-deficient hematite nanorods as high-performance and novel negative electrodes for flexible asymmetric supercapacitors. Adv Mater 26:3148–3155. https://doi.org/10.1002/adma.201305851

98. Li Y, Xu J, Feng T et al (2017) Fe$_2$O$_3$ nanoneedles on ultrafine nickel nanotube arrays as efficient anode for high-performance asymmetric supercapacitors. Adv Funct Mater 27:1606728. https://doi.org/10.1002/adfm.201606728

99. Zhang W, Zhao B, Yin Y et al (2016) Fe$_2$O$_3$-decorated millimeter-long vertically aligned carbon nanotube arrays as advanced anode materials for asymmetric supercapacitors with high energy and power densities. J Mater Chem A 4:19026–19036. https://doi.org/10.1039/C6TA07720J

100. Zeng Y, Han Y, Zhao Y et al (2015) Advanced Ti-doped Fe$_2$O$_3$@PEDOT core/shell anode for high-energy asymmetric supercapacitors. Adv Energy Mater 5:1402176. https://doi.org/10.1002/aenm.201402176

101. Zhao X, Johnston C, Grant PS (2009) A novel hybrid supercapacitor with a carbon nanotube cathode and an iron oxide/carbon nanotube composite anode. J Mater Chem 19:8755. https://doi.org/10.1039/b909779a

102. Chen JS, Zhu T, Yang XH et al (2010) Top-down fabrication of α-Fe$_2$O$_3$ single-crystal nanodiscs and microparticles with tunable porosity for largely improved lithium storage properties. J Am Chem Soc 132:13162–13164. https://doi.org/10.1021/ja1060438

103. Lei D, Zhang M, Qu B et al (2012) α-Fe$_2$O$_3$ nanowall arrays: hydrothermal preparation, growth mechanism and excellent rate performances for lithium ion batteries. Nanoscale 4:3422. https://doi.org/10.1039/c2nr30482a

104. Wang Z, Luan D, Madhavi S et al (2012) Assembling carbon-coated α-Fe$_2$O$_3$ hollow nanohorns on the CNT backbone for superior lithium storage capability. Energy Environ Sci 5:5252–5256. https://doi.org/10.1039/C1EE02831F

105. Yu L, Liu N, Wang X, Hu Z (2009) A general low-temperature CVD synthetic route to fabricate low-melting-point-metal compounds 1D nanostructures. J Alloys Compd 478:L21–L24. https://doi.org/10.1016/j.jallcom.2008.11.158

106. Liu X, Cui X, Chen Y et al (2015) Modulation of electromagnetic wave absorption by carbon shell thickness in carbon encapsulated magnetite nanospindles–poly(vinylidene fluoride) composites. Carbon 95:870–878. https://doi.org/10.1016/j.carbon.2015.09.036

107. Duan D, Fan K, Zhang D et al (2015) Nanozyme-strip for rapid local diagnosis of Ebola. Biosens Bioelectron 74:134–141. https://doi.org/10.1016/j.bios.2015.05.025

108. Baghayeri M, Veisi H (2015) Fabrication of a facile electrochemical biosensor for hydrogen peroxide using efficient catalysis of hemoglobin on the porous Pd@Fe$_3$O$_4$-MWCNT nanocomposite. Biosens Bioelectron 74:190–198. https://doi.org/10.1016/j.bios.2015.06.016

109. Du X, Wang C, Chen M et al (2009) Electrochemical performances of nanoparticle Fe$_3$O$_4$/activated carbon supercapacitor using KOH electrolyte solution. J Phys Chem C 113:2643–2646. https://doi.org/10.1021/jp8088269

110. Geng H, Zhou Q, Zheng J, Gu H (2014) Preparation of porous and hollow Fe$_3$O$_4$@C spheres as an efficient anode material for a high-performance Li-ion battery. RSC Adv 4:6430–6434. https://doi.org/10.1039/C3RA45300F

111. Zhou G, Wang D-W, Li F et al (2010) Graphene-wrapped Fe$_3$O$_4$ anode material with improved reversible capacity and cyclic stability for lithium ion batteries. Chem Mater 22:5306–5313. https://doi.org/10.1021/cm101532x

112. Duan Z-Q, Liu Y-T, Xie X-M et al (2016) h-BN nanosheets as 2D substrates to load 0D Fe$_3$O$_4$ nanoparticles: a hybrid anode material for lithium-ion batteries. Chem Asian J 11:828–833. https://doi.org/10.1002/asia.201501439

113. Santhosh Kumar R, Govindan K, Ramakrishnan S et al (2021) Fe$_3$O$_4$ nanorods decorated on polypyrrole/reduced graphene oxide for electrochemical detection of dopamine and photocatalytic degradation of acetaminophen. Appl Surf Sci 556:149765. https://doi.org/10.1016/j.apsusc.2021.149765

114. Wang J, Chen Q, Zeng C, Hou B (2004) Magnetic-field-induced growth of single-crystalline Fe$_3$O$_4$ nanowires. Adv Mater 16:137–140. https://doi.org/10.1002/adma.200306136

115. Shi Y-H, Wang K, Li H-H et al (2020) Fe$_3$O$_4$ nanoflakes-RGO composites: a high rate anode material for lithium-ion batteries. Appl Surf Sci 511:145465. https://doi.org/10.1016/j.apsusc.2020.145465

116. Yin C, Gong C, Chu J et al (2020) Ultrabroadband photodetectors up to 10.6 μm based on 2D Fe$_3$O$_4$ nanosheets. Adv Mater 32:2002237. https://doi.org/10.1002/adma.202002237

Lv *et al. Nanoscale Res Lett*   (2021) 16:138

Page 19 of 19

117. Ma Y, Huang J, Liu X et al (2017) 3D graphene-encapsulated hierarchical urchin-like Fe_3O_4 porous particles with enhanced lithium storage properties. Chem Eng J 327:678–685. https://doi.org/10.1016/j.cej.2017.06.147

118. Ma Y, Huang J, Lin L et al (2017) Self-assembly synthesis of 3D graphene-encapsulated hierarchical Fe_3O_4 nano-flower architecture with high lithium storage capacity and excellent rate capability. J Power Sources 365:98–108. https://doi.org/10.1016/j.jpowsour.2017.08.054

119. An Q, Lv F, Liu Q et al (2014) Amorphous vanadium oxide matrixes supporting hierarchical porous Fe_3O_4/graphene nanowires as a high-rate lithium storage anode. Nano Lett 14:6250–6256. https://doi.org/10.1021/nl5025694

120. Zhang W, Li X, Liang J et al (2016) One-step thermolysis synthesis of two-dimensional ultrafine Fe_3O_4 particles/carbon nanonetworks for high-performance lithium-ion batteries. Nanoscale 8:4733–4741. https://doi.org/10.1039/C5NR06843F

121. Li F, Shangguan E, Li J et al (2015) Influence of annealing temperature on the structure and electrochemical performance of the Fe_3O_4 anode material for alkaline secondary batteries. Electrochim Acta 178:34–44. https://doi.org/10.1016/j.electacta.2015.07.106

122. Tang NJ, Zhong W, Jiang HY et al (2004) Nanostructured magnetite (Fe_3O_4) thin films prepared by sol–gel method. J Magn Magn Mater 282:92–95. https://doi.org/10.1016/j.jmmm.2004.04.022

123. Xu J, Yang H, Fu W et al (2007) Preparation and magnetic properties of magnetite nanoparticles by sol–gel method. J Magn Magn Mater 309:307–311. https://doi.org/10.1016/j.jmmm.2006.07.037

124. Li C, Wei R, Xu Y et al (2014) Synthesis of hexagonal and triangular Fe_3O_4 nanosheets via seed-mediated solvothermal growth. Nano Res 7:536–543. https://doi.org/10.1007/s12274-014-0421-3

125. Mu J, Chen B, Guo Z et al (2011) Highly dispersed Fe_3O_4 nanosheets on one-dimensional carbon nanofibers: Synthesis, formation mechanism, and electrochemical performance as supercapacitor electrode materials. Nanoscale 3:5034. https://doi.org/10.1039/c1nr10972c

126. Wang L, Ji H, Wang S et al (2013) Preparation of Fe_3O_4 with high specific surface area and improved capacitance as a supercapacitor. Nanoscale 5:3793. https://doi.org/10.1039/c3nr00256j

127. Chen Y, Song B, Lu L, Xue J (2013) Ultra-small Fe_3O_4 nanoparticle decorated graphene nanosheets with superior cyclic performance and rate capability. Nanoscale 5:6797. https://doi.org/10.1039/c3nr01826a

128. Xiong QQ, Tu JP, Lu Y et al (2012) Synthesis of hierarchical hollow-structured single-crystalline magnetite (Fe_3O_4) microspheres: the highly powerful storage versus lithium as an anode for lithium ion batteries. J Phys Chem C 116:6495–6502. https://doi.org/10.1021/jp3002178

129. Chen JS, Zhang Y, Lou XW (2011) One-pot synthesis of uniform Fe_3O_4 nanospheres with carbon matrix support for improved lithium storage capabilities. ACS Appl Mater Interfaces 3:3276–3279. https://doi.org/10.1021/am201079z

130. Ooi F, DuChene JS, Qiu J et al (2015) A facile solvothermal synthesis of octahedral Fe_3O_4 nanoparticles. Small 11:2649–2653. https://doi.org/10.1002/smll.201401954

131. Jaramillo J, Boudouris BW, Barrero CA et al (2015) Design of superparamagnetic core-shell nanoparticles for enhanced performance of inverted polymer solar cells. ACS Appl Mater Interfaces 7:25061–25068. https://doi.org/10.1021/acsami.5b09686

132. Zhang F-J, Liu J, Zhang K et al (2012) A novel and simple approach for the synthesis of Fe_3O_4-graphene composite. Korean J Chem Eng 29:989–993. https://doi.org/10.1007/s11814-012-0031-2

133. Xu M, Liu M, Sun M et al (2016) Magnetic solid-phase extraction of phthalate esters (PAEs) in apparel textile by core–shell structured Fe_3O_4@silica@triblock-copolymer magnetic microspheres. Talanta 150:125–134. https://doi.org/10.1016/j.talanta.2015.12.027

134. Seo JY, Lee K, Praveenkumar R et al (2015) Tri-functionality of Fe_3O_4-embedded carbon microparticles in microalgae harvesting. Chem Eng J 280:206–214. https://doi.org/10.1016/j.cej.2015.05.122

135. Kang E, Jung YS, Cavanagh AS et al (2011) Fe_3O_4 Nanoparticles confined in mesocellular carbon foam for high performance anode materials for lithium-ion batteries. Adv Funct Mater 21:2430–2438. https://doi.org/10.1002/adfm.201002576

136. Kumar MP, Lathika LM, Mohanachandran AP, Rakhi RB (2018) A high-performance flexible supercapacitor anode based on polyaniline/Fe_3O_4 composite@carbon cloth. ChemistrySelect 3:3234–3240. https://doi.org/10.1002/slct.201800305

137. Wang L, Liu F, Pal A et al (2021) Ultra-small Fe_3O_4 nanoparticles encapsulated in hollow porous carbon nanocapsules for high performance supercapacitors. Carbon 179:327–336. https://doi.org/10.1016/j.carbon.2021.04.024

138. Shi W, Zhu J, Sim DH et al (2011) Achieving high specific charge capacitances in Fe_3O_4/reduced graphene oxide nanocomposites. J Mater Chem 21:3422–3427. https://doi.org/10.1039/C0JM03175E

139. Ma J, Guo X, Yan Y et al (2018) FeO_x-based materials for electrochemical energy storage. Adv Sci 5:1700986. https://doi.org/10.1002/advs.201700986

140. Zhou J, Song H, Ma L, Chen X (2011) Magnetite/graphene nanosheet composites: interfacial interaction and its impact on the durable high-rate performance in lithium-ion batteries. RSC Adv 1:782–791. https://doi.org/10.1039/C1RA00402F

141. Luo J, Liu J, Zeng Z et al (2013) Three-dimensional graphene foam supported Fe_3O_4 lithium battery anodes with long cycle life and high rate capability. Nano Lett 13:6136–6143. https://doi.org/10.1021/nl403461n

142. Kumar R, Soam A, Hossain R et al (2020) Carbon coated iron oxide (CC-IO) as high performance electrode material for supercapacitor applications. J Energy Storage 32:101737. https://doi.org/10.1016/j.est.2020.101737

143. Xu J-L, Zhang X, Miao Y-X et al (2021) In-situ plantation of Fe_3O_4@C nanoparticles on reduced graphene oxide nanosheet as high-performance anode for lithium/sodium-ion batteries. Appl Surf Sci 546:149163. https://doi.org/10.1016/j.apsusc.2021.149163

144. Liu N, Li C, Xie H et al (2019) Doping graphene into monodispersed Fe_3O_4 microspheres with droplet microfluidics for enhanced electrochemical performance in lithium-ion batteries. Batteries Supercaps 2:49–54. https://doi.org/10.1002/batt.201800072

145. Ma F-X, Hu H, Wu HB et al (2015) Formation of uniform Fe_3O_4 hollow spheres organized by ultrathin nanosheets and their excellent lithium storage properties. Adv Mater 27:4097–4101. https://doi.org/10.1002/adma.201501130

146. Han W, Qin X, Wu J et al (2018) Electrosprayed porous Fe_3O_4/carbon microspheres as anode materials for high-performance lithium-ion batteries. Nano Res 11:892–904. https://doi.org/10.1007/s12274-017-1700-6

147. Su J, Cao M, Ren L, Hu C (2011) Fe_3O_4–graphene nanocomposites with improved lithium storage and magnetism properties. J Phys Chem C 115:14469–14477. https://doi.org/10.1021/jp201666s

148. Lee SH, Yu S-H, Lee JE et al (2013) Self-assembled Fe_3O_4 nanoparticle clusters as high-performance anodes for lithium ion batteries via geometric confinement. Nano Lett 13:4249–4256. https://doi.org/10.1021/nl401952h

149. Zeng Y, Yu M, Meng Y et al (2016) Iron-based supercapacitor electrodes: advances and challenges. Adv Energy Mater 6:1601053. https://doi.org/10.1002/aenm.201601053

150. Fan H, Niu R, Duan J et al (2016) Fe_3O_4@carbon nanosheets for all-solid-state supercapacitor electrodes. ACS Appl Mater Interfaces 8:19475–19483. https://doi.org/10.1021/acsami.6b05415

151. Zhu X, Hou D, Tao H, Li M (2020) Simply synthesized N-doped carbon supporting Fe_3O_4 nanocomposite for high performance supercapacitor. J Alloys Compd 821:153580. https://doi.org/10.1016/j.jallcom.2019.153580

152. Xu B, Zheng M, Tang H et al (2019) Iron oxide-based nanomaterials for supercapacitors. Nanotechnology 30:204002. https://doi.org/10.1088/1361-6528/ab009f

Publisher's Note

Springer Nature remains neutral with regard to jurisdictional claims in published maps and institutional affiliations.